Available online at www.sciencedirect.com
ScienceDirect
Computers and Mathematics with Applications 00 (2016) 1–28
Computers and Mathematics with Applications

A lattice-Boltzmann scheme of the Navier-Stokes equation on a three-dimensional cuboid lattice

Lian-Ping Wang[a,b,*], Haoda Min[a], Cheng Peng[a], Nicholas Geneva[a], Zhaoli Guo[b]

[a] *Department of Mechanical Engineering, 126 Spencer Laboratory, University of Delaware, Newark, Delaware 19716-3140, USA*
[b] *State Key Laboratory of Coal Combustion, Huazhong University of Science and Technology, Wuhan, P.R. China*

Abstract

The standard lattice-Boltzmann method (LBM) for fluid flow simulation is based on a square (in 2D) or a cubic (in 3D) lattice grids. Recently, two new lattice Boltzmann schemes have been developed on a 2D rectangular grid using the MRT (multiple-relaxation-time) collision model, either by adding a free parameter in the definition of moments or by extending the equilibrium moments. These models satisfy all isotropy conditions and are fully consistent to the Navier-Stokes equations. Here we developed a lattice Boltzmann model on a 3D cuboid lattice, namely, a lattice grid with different grid lengths in different spatial directions. We designed the moment equations, derived from our MRT-LBM model through the Chapman-Enskog analysis, to be fully consistent with the Navier-Stokes equations. A second-order term is added to the equilibrium moments in order to not only satisfy all isotropy conditions but also to better accommodate different values of shear and bulk viscosities. The form of the second-order term and the coefficients of the extended equilibrium moments are determined through an inverse design process. An additional benefit of the model is that the shear viscosity can be adjusted, independent of the stress-moment relaxation parameter, thus potentially improving the numerical stability of the model. The resulting cuboid MRT-LBM model is then validated through benchmark simulations using the laminar channel flow, the turbulent channel flow, and the 3D time-dependent, energy-cascading Taylor-Green vortex flow. The second-order accuracy of the proposed model is also demonstrated. The numerical simulations suggest that the aspect ratios to ensure numerical stability appear to be constrained at high flow Reynolds numbers, especially for turbulent flow simulations, which requires further investigation.

Keywords: lattice Boltzmann, cuboid lattice, MRT, Chapman-Enskog analysis, inverse design
PACS: code, code

1. Introduction

As a mesoscopic method based on the kinetic Boltzmann equation, the lattice Boltzmann method (LBM) has been developed rapidly in the last three decades. The basic idea of LBM is the realization that, in the continuum and incompressible limits, only a few conserved moments and a few non-conserved moments are required to reproduce the macroscopic hydrodynamic equations. In the LBM, only a few discrete, kinetic-particle velocities are used, and the kinetic velocities are fully coupled with the lattice grid in the physical space and the time step size, which makes the numerical implementation highly efficient when compared to other kinetic schemes. The nonlinear interactions

*Corresponding author.
Email address: lwang@udel.edu (L.-P. Wang), min@udel.edu (H. Min), cpengxpp@udel.edu (C. Peng), ngeneva@udel.edu (N. Geneva), zlguo@hust.edu.cn (Zhaoli Guo)

between kinetic particles are local and are modeled through a collision model, namely, the single-relaxation-time or Bhatnagar-Gross-Krook (BGK) collision, or the multiple-relaxation-time (MRT) collision. Although the method solves more variables than the conventional CFD methods based on solving directly the Navier-Stokes (N-S) equations, its high computational efficiency and flexibility in treating complex solid-fluid boundaries and fluid-fluid interfaces have made the method a viable alternative CFD method for many complex flow applications [1, 2, 3].

For many years, the standard lattice grids are adopted in most previous studies, namely, typically a square lattice for 2D flows and a cubic lattice for 3D flows. These simple lattice grids have a good grid geometric isotropy, but at the same time, limit the computational efficiency when LBM models are applied to non-isotropic and inhomogeneous flows, in particular, wall-bounded turbulent flows. In order to remove this drawback, several efforts have been made to incorporate a more general (*i.e.*, nonuniform or anisotropic) grid into LBM. These efforts could be divided into four groups. The first group utilizes spatial and temporal interpolation schemes to couple the inherent lattice grid with a general computation grid on which the hydrodynamic variables are solved [4, 5]. Although such implementations allow more flexibility of the computational grid structure [6], the accuracy of such two-grid implementations is still determined by the inherent standard lattice. Furthermore, the interpolations introduce additional numerical errors and artificial viscosity to the flow system being solved. The second group chooses to replace the exact streaming operation in LBM with a finite-difference scheme or other discretization schemes [7, 8], in order to remove the usual coupling between lattice space and lattice time. This type of implementations not only causes additional numerical diffusion and dissipation, but could be more complicated and computationally more expensive, *e.g.*, additional data communication may be required.

Different from the above, the third group incorporates directly a non-standard lattice grid such as a rectangular grid in 2D, by modifying the kinetic particle velocities to fit the lattice grid. The use of a rectangular grid immediately introduces anisotropy which must be corrected by a proper re-design of the collision operator. This approach preserves all the appealing features of the standard LBM, *i.e.,* the inherent simplicity, numerical accuracy, and computational efficiency. Bouzidi *et al.* [9] was the first to propose a D2Q9 LBM using anisotropic particle velocities to fit a rectangular lattice grid. Their LBM scheme made use of the MRT collision operator. They modified the definitions of moments and their model is almost consistent with the Navier-Stokes equations, except that the shear and bulk viscosities are not strictly isotropic when the grid aspect ratio differs from one, as shown in [10]. Similar attempts were made by Zhou who proposed two models with both BGK [11] and MRT [12] collision operators. However, neither of his models is consistent with the N-S equations [10, 13]. Hegele *et al.* [14] claimed that, for the standard D2Q9 lattice and D3Q19 lattice, the degrees of freedom are not enough to remove thenanisotropy resulting from the use of the non-isotropic lattice grid, when the BGK collision operator is used. Thus they suggested to extend these lattices to D2Q11 and D3Q23, respectively, to recover the N-S equations. Their D2Q11 model was indeed validated on a rectangular grid using the 2D Taylor-Green vortex flow. Lastly, a D3Q19 model with cuboid lattice is proposed by Jiang and Zhang for pore-scale simulation of fluid flow in porous media [15]. In their model, the anisotropy of viscosity is fixed by adopting different relaxation parameters in different spatial directions. Although in their model, the lattice length of the cuboid could be different in three directions, the aspect ratio can only be larger than 0.82 due to stability consideration. In this paper, the aspect ratio is always defined as the ratio of smallest lattice spacing in one spatial direction to the largest lattice spacing in another spatial direction, except stated otherwise. In addition, the order of accuracy of Jiang and Zhang's model was not stated.

Recently, Zong *et al.* [10] extended Bouzidi *et al.*'s model by introducing a parameter θ to reconfigure the two-dimensional energy-normal stress moment sub-space. For a given grid aspect ratio, a unique θ value is determined to restore the full isotropy condition required by the N-S equations. An alternative and more general LBM MRT model on a rectangular grid has been developed by Peng *et al.* [16] who instead incorporated stress components into the equilibrium moments to remove the anisotropy in the stress tensor resulting from the use of a rectangular lattice. Such an approach was previously used by Inamuro [17] to improve the stability of LBGK model, and later by Yoshino *et al.* [18] and Wang *et al.* [19] to treat non-Newtonian fluid flows. The generality of the extended-equilibrium approach has also been explored using the simpler BGK collision by Peng *et al.* [20] who in fact showed that even an LBGK model can be successfully extended to work on a rectangular grid. Such was not thought to be possible previously. The key in all these three successful models on a rectangular grid [10, 16, 20] is to combine new constraints and new adjustable parameters to satisfy all isotropy conditions required by the N-S equations.

The objective of the current paper is to develop a D3Q19 MRT LBM model on a general cuboid grid with grid spacing ratios given as $\delta_x : \delta_y : \delta_z = 1 : a : b$, using a D3Q19 lattice. The basic idea of the approach follows

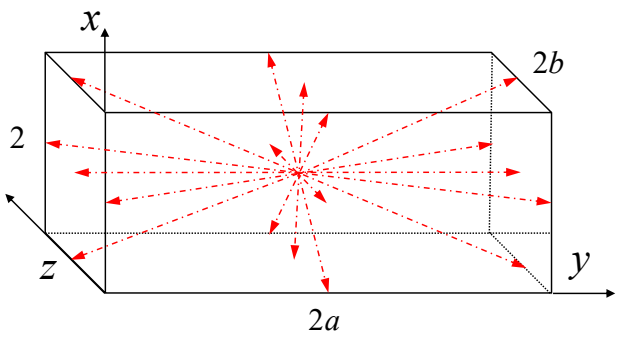

Figure 1: The illustration of D3Q19 cuboid lattice, the lattice size could be different in three directions.

closely the 2D extended-moment method described in [16]. The remainder of the paper is organized as follows. The derivation of the new model by the Chapman-Enskog analysis and an inverse design process is presented in Sec. 2. Careful validations of the model are provided in Sec. 3 using three different flows, namely, the transient laminar channel flow, the 3D time-dependent energy-cascading Taylor-Green vortex flow [22], and the turbulent channel flow. Finally, the order of accuracy of this model will be examined by the simulation results of the laminar channel flow and the 3D decaying Taylor-Green vortex flow.

2. The inverse design analysis of D3Q19 MRT-LBM with cuboid lattice

In this section, we shall design and derive a D3Q19 MRT LBM model on *a cuboid grid* that is consistent to the N-S equation with a non-uniform forcing $\mathbf{F} \equiv (F_x, F_y, F_z)$.

2.1. The basic model setup

For a cuboid lattice, the lattice spacings can be different in the three spatial directions. Without loss of the generality, we set the lattice spacing in the x direction to $\delta_x = 1$, and assume the grid spacing in y and z directions to be $a\delta_x$ and $b\delta_x$, respectively. Thus, a and b are defined as $a = \delta_y/\delta_x$, $b = \delta_z/\delta_x$, where δ_x $[m]$, δ_y $[m]$ and δ_z $[m]$ are the lattice sizes in the three directions, respectively. The physical units for key quantities are indicated to help validate the unit consistency of our model. A sketch of the cuboid lattice is shown in Fig. 1. Therefore, the corresponding discrete velocities on the D3Q19 cuboid lattice are

$$\mathbf{e}_i = \begin{cases} (0,0,0)\,c, & i = 0 \\ (\pm 1,0,0)\,c, (0,\pm a,0)\,c, (0,0,\pm b)\,c, & i = 1-6 \\ (\pm 1,\pm a,0)\,c, (\pm 1,0,\pm b)\,c, (0,\pm a,\pm b)\,c, & i = 7-18 \end{cases} \tag{1}$$

where $c = \delta_x/\delta_t$ $[m \cdot s^{-1}]$ is the non-zero lattice velocity component in the x direction, δ_t $[s]$ is the time step size.

The distribution functions in the cuboid-lattice LBM scheme evolve according to the same lattice Boltzmann equation (LBE) with the multiple relaxation time (MRT) collision, as

$$f_i(\mathbf{x} + \mathbf{e}_i\delta_t, t + \delta_t) - f_i(\mathbf{x}, t) = -\left[\mathbf{M}^{-1}\mathbf{S}\right]_{ij}\left[m_j(\mathbf{x}, t) - m_j^{eq}(\mathbf{x}, t)\right] + \Phi_i, \tag{2}$$

where f_i is the distribution function associated with the kinetic velocity $\mathbf{e}_i$, $\mathbf{x}$ and t are the spatial and time coordinates, respectively. The first term on the right hand side of Eq. (2) describes the MRT collision operator and the second term Φ_i $[kg \cdot m^{-3}]$ is used to represent the mesoscopic forcing term which accounts for the effect of macroscopic forcing $\mathbf{F} \equiv (F_x, F_y, F_z)$ $[kg \cdot m^{-2} \cdot s^{-2}]$. The components of Φ_i will be designed by an inverse design analysis.

The transformation matrix $\mathbf{M}$ converts the distribution functions f_i to the moments $\mathbf{m}$ by $\mathbf{m} = \mathbf{M}\mathbf{f}$, and vise versa $\mathbf{f} = \mathbf{M}^{-1}\mathbf{m}$, where $\mathbf{f}$ denotes a vector containing f_i. The equilibrium moments are denoted by $\mathbf{m}^{(eq)}$. For simplicity, the moments are defined in a manner similar to the standard D3Q19 MRT model [23]. Each discrete velocity $\mathbf{e}_i$ may have

different velocity magnitudes in the three spatial directions. In order to keep the same simple transformation matrix as in the cubic-lattice D3Q19 model, we first normalize the velocity components differently in different directions, namely, the transformation matrix and the moments are defined based on the normalized components e_{ix}/c, $e_{iy}/(a \cdot c)$, and $e_{iz}/(b \cdot c)$. The similar normalizations were used by Zhou [12] in his attempt to develop a D2Q9 rectangular-grid model. Therefore, the normalized components are identical to those in the standard cubic-lattice D3Q19 model. The transformation matrix is then written as [23]

$$\mathbf{M} = \begin{bmatrix}
1 & 1 & 1 & 1 & 1 & 1 & 1 & 1 & 1 & 1 & 1 & 1 & 1 & 1 & 1 & 1 & 1 & 1 & 1 \\
-30 & -11 & -11 & -11 & -11 & -11 & -11 & 8 & 8 & 8 & 8 & 8 & 8 & 8 & 8 & 8 & 8 & 8 & 8 \\
12 & -4 & -4 & -4 & -4 & -4 & -4 & 1 & 1 & 1 & 1 & 1 & 1 & 1 & 1 & 1 & 1 & 1 & 1 \\
0 & 1 & -1 & 0 & 0 & 0 & 0 & 1 & -1 & 1 & -1 & 1 & -1 & 1 & -1 & 0 & 0 & 0 & 0 \\
0 & -4 & 4 & 0 & 0 & 0 & 0 & 1 & -1 & 1 & -1 & 1 & -1 & 1 & -1 & 0 & 0 & 0 & 0 \\
0 & 0 & 0 & 1 & -1 & 0 & 0 & 1 & 1 & -1 & -1 & 0 & 0 & 0 & 0 & 1 & -1 & 1 & -1 \\
0 & 0 & 0 & -4 & 4 & 0 & 0 & 1 & 1 & -1 & -1 & 0 & 0 & 0 & 0 & 1 & -1 & 1 & -1 \\
0 & 0 & 0 & 0 & 0 & 1 & -1 & 0 & 0 & 0 & 0 & 1 & 1 & -1 & -1 & 1 & 1 & -1 & -1 \\
0 & 0 & 0 & 0 & 0 & -4 & 4 & 0 & 0 & 0 & 0 & 1 & 1 & -1 & -1 & 1 & 1 & -1 & -1 \\
0 & 2 & 2 & -1 & -1 & -1 & -1 & 1 & 1 & 1 & 1 & 1 & 1 & 1 & 1 & -2 & -2 & -2 & -2 \\
0 & -4 & -4 & 2 & 2 & 2 & 2 & 1 & 1 & 1 & 1 & 1 & 1 & 1 & 1 & -2 & -2 & -2 & -2 \\
0 & 0 & 0 & 1 & 1 & -1 & -1 & 1 & 1 & 1 & 1 & -1 & -1 & -1 & -1 & 0 & 0 & 0 & 0 \\
0 & 0 & 0 & -2 & -2 & 2 & 2 & 1 & 1 & 1 & 1 & -1 & -1 & -1 & -1 & 0 & 0 & 0 & 0 \\
0 & 0 & 0 & 0 & 0 & 0 & 0 & 1 & -1 & -1 & 1 & 0 & 0 & 0 & 0 & 0 & 0 & 0 & 0 \\
0 & 0 & 0 & 0 & 0 & 0 & 0 & 0 & 0 & 0 & 0 & 0 & 0 & 0 & 0 & 1 & -1 & -1 & 1 \\
0 & 0 & 0 & 0 & 0 & 0 & 0 & 0 & 0 & 0 & 0 & 1 & -1 & -1 & 1 & 0 & 0 & 0 & 0 \\
0 & 0 & 0 & 0 & 0 & 0 & 0 & 1 & -1 & 1 & -1 & -1 & 1 & -1 & 1 & 0 & 0 & 0 & 0 \\
0 & 0 & 0 & 0 & 0 & 0 & 0 & -1 & -1 & 1 & 1 & 0 & 0 & 0 & 0 & 1 & -1 & 1 & -1 \\
0 & 0 & 0 & 0 & 0 & 0 & 0 & 0 & 0 & 0 & 0 & 1 & 1 & -1 & -1 & -1 & -1 & 1 & 1
\end{bmatrix}, \tag{3}$$

where the row vectors of $\mathbf{M}$ are orthogonal with each other, so are the column vectors in the inverse matrix $\mathbf{M^{-1}}$ [24]. The individual moments thus derived by $\mathbf{m} = \mathbf{Mf}$ are denoted as

$$\mathbf{m} = \left|\tilde{\rho}, e, \varepsilon, j_x, q_x, j_y, q_y, j_z, q_z, 3p_{xx}, \pi_{xx}, p_{ww}, \pi_{ww}, p_{xy}, p_{yz}, p_{xz}, m_x, m_y, m_z\right\rangle, \tag{4}$$

where $\tilde{\rho}$ $[kg \cdot m^{-3}]$ is the zeroth-order moment representing local density fluctuation, namely, $\tilde{\rho} = \rho - \rho_0 \equiv \delta\rho$ (ρ and ρ_0 are the density and the average density, respectively); e $[kg \cdot m^{-1} \cdot s^{-2}]$ is a second-order moment related to the energy; ε $[kg \cdot m \cdot s^{-4}]$ is a fourth-order moment associated with the square of energy; j_x, j_y, j_z $[kg \cdot m^{-2} \cdot s^{-1}]$ are the three first-order moments connected to the momentum in x, y and z direction, respectively; q_x, q_y, q_z $[kg \cdot s^{-3}]$ are three third-order moments related to the energy flux in x, y and z direction, respectively; p_{xx}, p_{ww} $[kg \cdot m^{-1} \cdot s^{-2}]$ are two second-order moments corresponding to the normal stress components; p_{xy}, p_{yz}, p_{xz} $[kg \cdot m^{-1} \cdot s^{-2}]$ are the other three second-order moments related to the shear-stress components; m_x, m_y, m_z are all third-order moments that can be regarded as the normal stress flux; π_{xx} and π_{ww} $[kg \cdot m \cdot s^{-4}]$ are the fourth-order moments derived from products between energy mode and normal stress mode. Note that the density has been partitioned as in [25] to better reproduce the incompressible N-S equations. In summary, in the D3Q19 model, we have one zeroth-order moment ($\tilde{\rho}$), three first-order moments (j_x, j_y, j_z), six second-order moments ($e, p_{xx}, p_{ww}, p_{xy}, p_{yz}, p_{xz}$), six third-order moments ($q_x, q_y, q_z, m_x, m_y, m_z$), and three fourth-order moments ($\varepsilon, \pi_{xx}, \pi_{ww}$). These are all the independent moments that can be formed.

As we shall show later, all the moments at the third order or below can be uniquely determined in our inverse design process, while the three fourth-order moments are irrelevant to the N-S equations.

The diagonal relaxation matrix $\mathbf{S}$ specifies all dimensionless relaxation parameters

$$\mathbf{S} = diag(s_{\tilde{\rho}}, s_e, s_\varepsilon, s_j, s_q, s_j, s_q, s_j, s_q, s_n, s_\pi, s_n, s_\pi, s_c, s_c, s_c, s_m, s_m, s_m), \tag{5}$$

where $s_{\tilde{\rho}}$ is the relaxation parameter for the zeroth-order moment ($\tilde{\rho}$); s_j is the relaxation parameter for the first-order moments (j_x, j_y, j_z); three relaxation parameters are introduced for the six second-order moments: s_e for energy (e), s_n for the normal-stress moments (p_{xx}, p_{ww}), and s_c for the shear-stress moments (p_{xy}, p_{yz}, p_{xz}); two relaxation

parameters are used for the six third-order moments: s_q for energy flux moments (q_x, q_y, q_z) and s_m for normal-stress flux moments (m_x, m_y, m_z); finally, two relaxation parameters are specified for the three fourth-order moments: s_ε for energy square moment (ε) and s_π for the energy-stress coupling terms (π_{xx}, π_{ww}). As mentioned in the introduction, we need to overcome the anisotropic transport coefficients that are originated by the anisotropic lattice velocities, in order to reproduce the N-S equations. In this work, we follow the same idea as in [16], namely, the equilibrium moments are extended to include a higher-oder term as $\mathbf{m}^{(eq)} = \mathbf{m}^{(eq,0)} + \epsilon\mathbf{m}^{(eq,1)}$, where ϵ is a small parameter that is proportional to the Knudsen number. The higher-order term $\epsilon\mathbf{m}^{(eq,1)}$ will be expressed in terms of stress components.

2.2. The Chapman-Enskog analysis and inverse design

Next, a detailed Chapman-Enskog analysis will be performed to design the components of the equilibrium moment $\mathbf{m}^{(eq)}$ and the mesoscopic forcing term $\mathbf{\Phi}$. Following the standard procedure, the Taylor expansion with respect to time and location is applied to $f_i(\mathbf{x} + \mathbf{e}_i\delta_t, t + \delta_t)$ in Eq. (2). After multiplying by $\mathbf{M}/\delta_t$, we obtain

$$\left(\mathbf{I}\partial_t + \hat{\mathbf{C}}_\alpha\nabla_\alpha\right)\mathbf{m} + \frac{\delta_t}{2}\left(\mathbf{I}\partial t + \hat{\mathbf{C}}_\alpha\nabla_\alpha\right)^2\mathbf{m} = -\frac{\mathbf{S}}{\delta_t}\left(\mathbf{m} - \mathbf{m}^{(eq)}\right) + \mathbf{\Psi}, \tag{6}$$

where $\mathbf{I}$ is an identity matrix, $\mathbf{\Psi} \equiv \mathbf{M}\mathbf{\Phi}/\delta_t$ denotes the moments associated with the forcing term, ∂_t stands for the time derivative, ∇_α with $\alpha = x$, y, or z denotes the spatial derivatives, and $\hat{\mathbf{C}}_\alpha \equiv \mathbf{M}diag(e_{i\alpha})\mathbf{M^{-1}}$. The following multiscale expansion is now applied to $\mathbf{m}$, $\mathbf{m}^{(eq)}$, ∂_t, ∇_α, and $\mathbf{\Psi}$:

$$\mathbf{m} = \mathbf{m}^{(0)} + \epsilon\,\mathbf{m}^{(1)} + \epsilon^2\mathbf{m}^{(2)} + ..., \tag{7a}$$

$$\mathbf{m}^{(eq)} = \mathbf{m}^{(eq,0)} + \epsilon\,\mathbf{m}^{(eq,1)}, \tag{7b}$$

$$\partial_t = \epsilon\,\partial_{t1} + \epsilon^2\partial_{t2}, \tag{7c}$$

$$\nabla_\alpha = \epsilon\,\nabla_{1\alpha}, \tag{7d}$$

$$\mathbf{\Psi} = \epsilon\,\mathbf{\Psi}^{(1)}. \tag{7e}$$

Once again, the most significant difference here is that the multiscale expansion is also applied to the equilibrium moments $\mathbf{m}^{(eq)}$. Substituting Eq. (7) into Eq. (6) and rearranging the equation according to $O(\epsilon)$, we obtain the following three equations

$$O(1):\ \mathbf{m}^{(0)} = \mathbf{m}^{(eq,0)}, \tag{8a}$$

$$O(\epsilon):\ \left(\mathbf{I}\partial_{t1} + \hat{\mathbf{C}}_\alpha\partial_{1\alpha}\right)\mathbf{m}^{(0)} = -\frac{\mathbf{S}}{\delta_t}\left(\mathbf{m}^{(1)} - \mathbf{m}^{(eq,1)}\right) + \mathbf{\Psi}^{(1)}, \tag{8b}$$

$$O(\epsilon^2):\ \partial_{t2}\mathbf{m}^{(0)} + \left(\mathbf{I}\partial_{t1} + \hat{\mathbf{C}}_\alpha\partial_{1\alpha}\right)\left[\left(\mathbf{I} - \frac{\mathbf{S}}{2}\right)\mathbf{m}^{(1)} + \frac{\mathbf{S}}{2}\mathbf{m}^{(eq,1)} + \frac{\delta_t}{2}\mathbf{\Psi}^{(1)}\right] = -\frac{\mathbf{S}}{\delta_t}\mathbf{m}^{(2)}. \tag{8c}$$

Each equation in Eq. (8) is a vector equation containing 19 scalar-moment equations. Based on the ordering of moments defined in Eq. (4), the first row of Eq. (8b) and (8c) should correspond to the continuity equation. The 4^{th}, 6^{th} and 8^{th} row of Eq. (8b) and (8c) should correspond to the hydrodynamic momentum equations in x, y and z directions, respectively.

Since density is a conserved moment, we set $\tilde{\rho}^{(0)} = \tilde{\rho}^{(eq,0)} = \delta\rho$ and $s_{\tilde{\rho}} = 0$. Therefore, $\tilde{\rho}^{(k)} = 0$ for $k \geq 1$. The first row of Eq. (8b) thus becomes

$$\partial_{t1}\delta\rho + \partial_{1x}j_x^{(0)} + a\partial_{1y}j_y^{(0)} + b\partial_{1z}j_z^{(0)} = \frac{s_{\tilde{\rho}}}{\delta_t}\tilde{\rho}^{(eq,1)} + \Psi_1^{(1)}, \tag{9}$$

which should reproduce the continuity equation at $O(\epsilon)$ to the leading order

$$\partial_{t1}\delta\rho + \partial_{1x}(\rho_0 u) + \partial_{1y}(\rho_0 v) + \partial_{1z}(\rho_0 w) = 0. \tag{10}$$

Therefore, $j_x^{(0)} = \rho_0 u$, $j_y^{(0)} = \rho_0 v/a$, $j_z^{(0)} = \rho_0 w/b$. Since the density should not be affected by the forcing, we must have $\Psi_1^{(1)} = 0$, and thus $\tilde{\rho}^{(eq,1)} = 0$.

Likewise, the $4^{th}, 6^{th}$ and 8^{th} rows of Eq. (8b)

$$\partial_{t1}(\rho_0 u) + \partial_{1x}\left(\frac{10}{19}c^2\delta\rho + \frac{1}{57}e^{(0)} + \frac{1}{3}p_{xx}^{(0)}\right) + a\partial_{1y}\left(p_{xy}^{(0)}\right) + b\partial_{1z}\left(p_{xz}^{(0)}\right) = -\frac{s_j}{\delta_t}\left(j_x^{(1)} - j_x^{(eq,1)}\right) + \Psi_4^{(1)}, \tag{11a}$$

$$\partial_{t1}\left(\frac{\rho_0 v}{a}\right) + a\partial_{1y}\left(\frac{10}{19}c^2\delta\rho + \frac{1}{57}e^{(0)} - \frac{1}{6}p_{xx}^{(0)} + \frac{1}{2}p_{ww}^{(0)}\right) + \partial_{1x}\left(p_{xy}^{(0)}\right) + b\partial_{1z}\left(p_{yz}^{(0)}\right) = -\frac{s_j}{\delta_t}\left(j_y^{(1)} - j_y^{(eq,1)}\right) + \Psi_6^{(1)}, \tag{11b}$$

$$\partial_{t1}\left(\frac{\rho_0 w}{b}\right) + b\partial_{1z}\left(\frac{10}{19}c^2\delta\rho + \frac{1}{57}e^{(0)} - \frac{1}{6}p_{xx}^{(0)} - \frac{1}{2}p_{ww}^{(0)}\right) + \partial_{1x}\left(p_{xz}^{(0)}\right) + a\partial_{1y}\left(p_{yz}^{(0)}\right) = -\frac{s_j}{\delta_t}\left(j_z^{(1)} - j_z^{(eq,1)}\right) + \Psi_8^{(1)}, \tag{11c}$$

must match the following Euler momentum equations

$$\partial_{t1}(\rho_0 u) + \partial_{1x}\left(p + \rho_0 u^2\right) + \partial_{1y}(\rho_0 uv) + \partial_{1z}(\rho_0 uw) = F_x^{(1)}, \tag{12a}$$

$$\partial_{t1}(\rho_0 v) + \partial_{1y}\left(p + \rho_0 v^2\right) + \partial_{1x}(\rho_0 uv) + \partial_{1z}(\rho_0 vw) = F_y^{(1)}, \tag{12b}$$

$$\partial_{t1}(\rho_0 w) + \partial_{1z}\left(p + \rho_0 w^2\right) + \partial_{1x}(\rho_0 uw) + \partial_{1y}(\rho_0 vw) = F_z^{(1)}. \tag{12c}$$

In Eq. (12) the pressure is expressed as $p = \delta\rho c_s^2$, where c_s $[m \cdot s^{-1}]$ is the speed of sound. Consistency of the left hand sides of Eq. (11) and Eq. (12) leads to the following results

$$e^{(0)} = 19\delta\rho(c_s^2 + \frac{c_s^2}{a^2} + \frac{c_s^2}{b^2} - \frac{30}{19}c^2) + 19\rho_0(u^2 + \frac{v^2}{a^2} + \frac{w^2}{b^2}), \tag{13a}$$

$$p_{xx}^{(0)} = \delta\rho(2c_s^2 - \frac{c_s^2}{a^2} - \frac{c_s^2}{b^2}) + \rho_0(2u^2 - \frac{v^2}{a^2} - \frac{w^2}{b^2}), \tag{13b}$$

$$p_{ww}^{(0)} = \delta\rho c_s^2\frac{b^2 - a^2}{a^2 b^2} + \rho_0(\frac{v^2}{a^2} - \frac{w^2}{b^2}), \tag{13c}$$

$$p_{xy}^{(0)} = \frac{\rho_0 uv}{a}, \quad p_{xz}^{(0)} = \frac{\rho_0 uw}{b}, \quad p_{yz}^{(0)} = \frac{\rho_0 vw}{ab}. \tag{13d}$$

And a comparison of the right hand sides of Eq. (11) and Eq. (12) yields

$$-\frac{s_j}{\delta_t}j_x^{(1)} + \frac{s_j}{\delta_t}j_x^{(eq,1)} + \Psi_4^{(1)} = F_x^{(1)}, \tag{14a}$$

$$-\frac{s_j}{\delta_t}j_y^{(1)} + \frac{s_j}{\delta_t}j_y^{(eq,1)} + \Psi_6^{(1)} = \frac{F_y^{(1)}}{a}, \tag{14b}$$

$$-\frac{s_j}{\delta_t}j_z^{(1)} + \frac{s_j}{\delta_t}j_z^{(eq,1)} + \Psi_8^{(1)} = \frac{F_z^{(1)}}{b}. \tag{14c}$$

Next, we proceed to compare the moment equations on the order of $O\left(\epsilon^2\right)$ with the N-S equations. For simplicity, we define

$$\mathbf{A} \equiv \left(\mathbf{I} - \frac{\mathbf{S}}{2}\right)\mathbf{m}^{(1)} + \frac{\mathbf{S}}{2}\mathbf{m}^{(eq,1)} + \frac{\delta_t}{2}\mathbf{\Psi}^{(1)}, \tag{15}$$

which simplifies Eq. (8c) to

$$O\left(\epsilon^2\right) : \partial_{t2}\mathbf{m}^{(0)} + (\mathbf{I}\partial_{t1} + \hat{\mathbf{C}}_\alpha\partial_{1\alpha})\mathbf{A} = -\frac{\mathbf{S}}{\delta_t}\mathbf{m}^{(2)}. \tag{16}$$

Since we have shown that $\rho_1^{(1)} = \rho_1^{(eq,1)} = 0$ and $\Psi_1^{(1)} = 0$, it follows that the first element of $\mathbf{A}$, namely, A_1, should also be zero. Then the 1^{st} row of Eq. (16) reads

$$\partial_{t2}\delta\rho + \partial_{1x}A_4 + \partial_{1y}A_6 + \partial_{1z}A_8 = 0. \tag{17}$$

The above equation should match with the continuity equation at $O\left(\epsilon^2\right)$, namely, $\partial_{t2}\delta\rho = 0$. Therefore, $A_4 = A_6 = A_8 = 0$, and the following three constraints are obtained

$$A_4 = \left(1 - \frac{s_j}{2}\right) j_x^{(1)} + \frac{s_j}{2} j_x^{(eq,1)} + \frac{\delta_t}{2}\Psi_4^{(1)} = 0, \tag{18a}$$

$$A_6 = \left(1 - \frac{s_j}{2}\right) j_y^{(1)} + \frac{s_j}{2} j_y^{(eq,1)} + \frac{\delta_t}{2}\Psi_6^{(1)} = 0, \tag{18b}$$

$$A_8 = \left(1 - \frac{s_j}{2}\right) j_z^{(1)} + \frac{s_j}{2} j_z^{(eq,1)} + \frac{\delta_t}{2}\Psi_8^{(1)} = 0. \tag{18c}$$

Eqs. (14) and (18) together lead to

$$j_x^{(1)} = -F_x^{(1)}\delta_t/2, \quad j_y^{(1)} = -F_y^{(1)}\delta_t/2a, \quad j_z^{(1)} = -F_z^{(1)}\delta_t/2b. \tag{19}$$

The next order equilibrium moments $j_{x,y,z}^{(eq,1)}$ and the forcing term $\Psi_{4,6,8}^{(1)}$ are not easily separable since they are coupled in both Eqs. (14) and (18). However, they do not appear in our later derivation. For convenience, we can simply set $j_{x,y,z}^{(eq,1)} = 0$, which then leads to $\Psi_4^{(1)} = (1 - 0.5s_j)F_x^{(1)}$, $\Psi_6^{(1)} = (1 - 0.5s_j)F_y^{(1)}/a$ and $\Psi_8^{(1)} = (1 - 0.5s_j)F_z^{(1)}/b$.

Now the 4^{th}, 6^{th} and 8^{th} rows of Eq. (8c)

$$\partial_{t2}(\rho_0 u) + \partial_{1x}\left(\frac{A_2}{57} + \frac{A_{10}}{3}\right) + a\partial_{1y}A_{14} + a\partial_{1z}A_{16} = -\frac{s_j}{\delta_t} j_x^{(2)}, \tag{20a}$$

$$\partial_{t2}\left(\frac{\rho_0 v}{a}\right) + \partial_{1y}\left(\frac{aA_2}{57} - \frac{aA_{10}}{6} + \frac{aA_{12}}{2}\right) + \partial_{1x}A_{14} + b\partial_{1z}A_{15} = -\frac{s_j}{\delta_t} j_y^{(2)}, \tag{20b}$$

$$\partial_{t2}\left(\frac{\rho_0 w}{b}\right) + \partial_{1z}\left(\frac{bA_2}{57} - \frac{bA_{10}}{6} - \frac{bA_{12}}{2}\right) + \partial_{1x}A_{16} + a\partial_{1y}A_{15} = -\frac{s_j}{\delta_t} j_z^{(2)}, \tag{20c}$$

are compared to the N-S equations, namely,

$$\partial_{t2}(\rho_0 u) - \partial_{1x}\left[\mu^V \nabla_1 \mathbf{u} + \mu\left(\frac{4}{3}\partial_{1x}u - \frac{2}{3}\partial_{1y}v - \frac{2}{3}\partial_{1z}w\right)\right] - \mu\partial_{1y}\left(\partial_{1y}u + \partial_{1x}v\right) - \mu\partial_{1z}\left(\partial_{1z}u + \partial_{1x}w\right) = 0, \tag{21a}$$

$$\partial_{t2}(\rho_0 v) - \partial_{1y}\left[\mu^V \nabla_1 \mathbf{u} + \mu\left(\frac{4}{3}\partial_{1y}v - \frac{2}{3}\partial_{1x}u - \frac{2}{3}\partial_{1z}w\right)\right] - \mu\partial_{1x}\left(\partial_{1y}u + \partial_{1x}v\right) - \mu\partial_{1z}\left(\partial_{1z}v + \partial_{1y}w\right) = 0, \tag{21b}$$

$$\partial_{t2}(\rho_0 w) - \partial_{1y}\left[\mu^V \nabla_1 \mathbf{u} + \mu\left(\frac{4}{3}\partial_{1z}w - \frac{2}{3}\partial_{1y}v - \frac{2}{3}\partial_{1x}u\right)\right] - \mu\partial_{1y}\left(\partial_{1y}w + \partial_{1z}v\right) - \mu\partial_{1x}\left(\partial_{1z}u + \partial_{1x}w\right) = 0, \tag{21c}$$

where $\nabla_1 \mathbf{u} \equiv \partial_{1x}u + \partial_{1y}v + \partial_{1z}w$, μ $[kg \cdot m^{-1} \cdot s^{-1}]$ and μ^V $[kg \cdot m^{-1} \cdot s^{-1}]$ are the dynamic shear and bulk viscosity, respectively. In order for Eq. (20) to be consistent with Eq. (21), we must set $j_x^{(2)} = j_y^{(2)} = j_z^{(2)} = 0$. Furthermore, A_2, A_{10}, A_{12}, A_{14}, A_{15} and A_{16} can be determined in terms of viscosity coefficients and velocity gradients as

$$A_2 = -\frac{19\mu}{3}\left(\omega_1 + \frac{\omega_2}{a^2} + \frac{\omega_3}{b^2}\right) - 19\kappa_1\mu^V\nabla_1\mathbf{u}, \tag{22a}$$

$$A_{10} = -\frac{\mu}{3}\left(2\omega_1 - \frac{\omega_2}{a^2} - \frac{\omega_3}{b^2}\right) - (3 - \kappa_1)\,\mu^V\nabla_1\mathbf{u}, \tag{22b}$$

$$A_{12} = -\frac{\mu}{3}\left(\frac{\omega_2}{a^2} - \frac{\omega_3}{b^2}\right) - \kappa_2\mu^V\nabla_1\mathbf{u}, \tag{22c}$$

$$A_{14} = -\frac{\mu}{a}\left(\partial_{1y}u + \partial_{1x}v\right), \tag{22d}$$

$$A_{15} = -\frac{\mu}{ab}\left(\partial_{1y}w + \partial_{1z}v\right), \tag{22e}$$

$$A_{16} = -\frac{\mu}{b}\left(\partial_{1z}u + \partial_{1x}w\right), \tag{22f}$$

where $\omega_1 = 4\partial_{1x}u - 2\partial_{1y}v - 2\partial_{1z}w$, $\omega_2 = 4\partial_{1y}v - 2\partial_{1x}u - 2\partial_{1z}w$, $\omega_3 = 4\partial_{1z}w - 2\partial_{1y}v - 2\partial_{1x}u$, $\kappa_1 = 1/a^2 + 1/b^2 + 1$ and $\kappa_2 = 1/a^2 - 1/b^2$. Recall that in Eq. (15) we defined $\mathbf{A}$ as functions of equilibrium moments $\mathbf{m}^{(eq,1)}$ and non-equilibrium moments $\mathbf{m}^{(1)}$ and the mesoscopic forcing terms $\mathbf{\Psi}$. Re-arranging Eq. (8b), $\mathbf{m}^{(1)}$ can be obtained in terms

of equilibrium moments and the forcing term as

$$\mathbf{m}^{(1)} = \delta_t \mathbf{S}^{-1}\left[\mathbf{\Psi}^{(1)} - \left(I\partial_{t1} + \hat{C}_\alpha \partial_{1\alpha}\right)\mathbf{m}^{(eq,0)}\right] + \mathbf{m}^{(eq,1)}. \tag{23}$$

Substituting Eq. (23) into Eq. (15), we can express $\mathbf{A}$ as functions of equilibrium moments and forcing components as

$$\mathbf{A} = \delta_t \mathbf{S}^{-1}\mathbf{\Psi}^{(1)} + \mathbf{m}^{(eq,1)} - \left(\mathbf{S}^{-1} - \frac{\mathbf{I}}{2}\right)\left(\mathbf{I}\partial_{t1} + \hat{\mathbf{C}}_\alpha \partial_{1\alpha}\right)\mathbf{m}^{(eq,0)}, \tag{24}$$

and it is important to recognize that, from Eq. (24), the six components of $m_i^{(eq,1)}$ involved in Eqs. (20) and (22) are all related to the second-oder moments.

A comparison of Eq. (22) and Eq. (24) now allows us to design $\mathbf{m}^{(eq)}$ and $\mathbf{\Psi}$ so that the hydrodynamic equations can be satisfied. It is also important to note that the forcing term is introduced to reproduce the macroscopic force, without other impacts on the N-S equations. Therefore, we abide by two basic considerations: (a) all terms that contain macroscopic force $\mathbf{F}$ and mesoscopic forcing terms $\mathbf{\Psi}$ should balance and (b) they should be treated separately. In other words, the model should still work properly if the forcing terms are not present in the LBE and the N-S equations. These considerations lead to a set of constraints that allow us to derive the most general mesoscopic forcing formulation. The details are presented in Min *et al.* [27] when the general forcing formulations for three D2Q9 models (on both the square and rectangular lattice grids) are considered. The similar inverse design process is conducted here. The final results for our D3Q19 cuboid-grid model based on the above considerations are

$$\begin{cases} q_x^{(0)} = \gamma c^2 \rho_0 u, \\ q_y^{(0)} = \left(a^2\kappa_3 - 4\right)c^2\rho_0 v/a, \\ q_z^{(0)} = \left(b^2\kappa_3 - 4\right)c^2\rho_0 w/b, \\ m_x^{(0)} = 0, \\ m_y^{(0)} = 0, \\ m_z^{(0)} = 0, \end{cases} \qquad \begin{cases} \epsilon m_2^{(eq,1)} = \rho_0\delta_t c^2\left(h_{11}\partial_x u + h_{12}\partial_y v + h_{13}\partial_z w\right), \\ \epsilon m_{10}^{(eq,1)} = \rho_0\delta_t c^2\left(h_{21}\partial_x u + h_{22}\partial_y v + h_{23}\partial_z w\right), \\ \epsilon m_{12}^{(eq,1)} = \rho_0\delta_t c^2\left(h_{31}\partial_x u + h_{32}\partial_y v + h_{33}\partial_z w\right), \\ \epsilon m_{14}^{(eq,1)} = \rho_0\delta_t c^2\lambda\left(\partial_y u + \partial_x v\right)/a, \\ \epsilon m_{15}^{(eq,1)} = \rho_0\delta_t c^2\left[s_c^*\kappa_3\left(a^2b^2 - a^2\right)/10 + \lambda\right]\left(\partial_z v + \partial_y w\right)/(ab), \\ \epsilon m_{16}^{(eq,1)} = \rho_0\delta_t c^2\left[s_c^*\kappa_3\left(b^2 - a^2\right)/10 + \lambda\right]\left(\partial_x w + \partial_z u\right)/b, \end{cases} \tag{25}$$

where $\kappa_3 = (\gamma + 4)$, $s_e^* = (2 - s_e)/(2s_e)$, $s_n^* = (2 - s_n)/(2s_n)$, and $s_c^* = (2 - s_c)/(2s_c)$. Note that γ is the coefficient in $q_x^{(0)}$, the energy flux in the x direction. In the current model, γ is an adjustable parameter. However, in the MRT LBM model on the cubic lattice, γ is not adjustable [23, 24]. Previously, in several LBM models on a rectangular grid [9, 10, 12, 16, 27], γ is indeed shown to be a free parameter. The coefficients for other two energy flux moments, $q_y^{(0)}$ and $q_z^{(0)}$, are not free but depend on γ because they are constrained by isotropy requirements, namely, to achieve necessary balance of the transport coefficients associated with different velocity gradients in Eq. (22d) to Eq. (22f).

It is reminded that the formulations of six $m_i^{(eq,1)}$ moments shown in Eq. (25) are derived from the consistency and isotropy considerations with the N-S equations. However, they also bring in additional benefits. For example, λ and h_{ij} are the coefficients in $\epsilon m_i^{(eq,1)}$ as indicated in Eq. (25). Some of these coefficients provide a benefit to adjust both shear and bulk viscosity which in this model are given as

$$\mu = \rho_0\delta_t c^2\left[\frac{a^2 s_c^*(4+\gamma)}{10} - \lambda\right], \tag{26a}$$

$$\mu^V = \rho_0\delta_t c^2\left[s_e^*\frac{15\left(1 - \kappa_1 c_s^2\right) + (4+\gamma)\left(1 + a^2 + b^2\right)}{15\kappa_1} - \frac{h_{11} + h_{12} + h_{13}}{57\kappa_1}\right]. \tag{26b}$$

We can conclude from Eq. (26) that the relaxation time s_c, s_e are no longer uniquely determined by viscosity since λ and h_{ij} are also adjustable. Therefore, for given physical shear and bulk viscosities, we could set s_c, s_e to any value between 0 and 2. This is not possible in the standard LBM MRT model.

It is also important to note that the expressions of both the shear and bulk viscosities in Eq. (26) are consistent with the expressions in the standard D3Q19 MRT LBM with the cubic lattice [23] if we set $a = b = 1$, $\gamma = -2/3$, $\kappa_1 = 3$, and all extended equilibrium moments to zero, namely, $h_{ij} = \lambda = 0$.

The consistency and isotropy considerations specify the value of the coefficients h_{ij} in $\epsilon m^{(eq,1)}_{2,10,12}$ shown in Eq. (25). They are determined explicitly as

$$h_{ij} = g_{ij} + \begin{bmatrix} 19s_e^*\left(\frac{\kappa_3}{5} - \kappa_1\frac{c_s^2}{c^2} + 1\right) & 19s_e^*\left(\frac{a^2\kappa_3}{5} - \kappa_1\frac{c_s^2}{c^2} + 1\right) & 19s_e^*\left(\frac{b^2\kappa_3}{5} - \kappa_1\frac{c_s^2}{c^2} + 1\right) \\ s_n^*\left[\frac{6-\gamma}{5} + (\kappa_1 - 3)\frac{c_s^2}{c^2}\right] & s_n^*\left[\frac{a^2\kappa_3}{10} + (\kappa_1 - 3)\frac{c_s^2}{c^2} - 1\right] & s_n^*\left[\frac{b^2\kappa_3}{10} + (\kappa_1 - 3)\frac{c_s^2}{c^2} - 1\right] \\ -s_n^*\frac{c_s^2}{c^2}\kappa_2 & -s_n^*\left(\frac{a^2\kappa_3}{10} + \frac{c_s^2}{c^2}\kappa_2 - 1\right) & s_n^*\left(\frac{b^2\kappa_3}{10} - \frac{c_s^2}{c^2}\kappa_2 - 1\right) \end{bmatrix}, \tag{27}$$

where g_{ij} are calculated as

$$g_{ij} = \frac{1}{\rho_0\delta_t c^2}\begin{bmatrix} \frac{38(\kappa_1-3)}{3}\mu - 19\kappa_1\mu^V & \frac{38\left(a^2\kappa_1-3\right)}{3a^2}\mu - 19\kappa_1\mu^V & \frac{38\left(b^2\kappa_1-3\right)}{3b^2}\mu - 19\kappa_1\mu^V \\ -\frac{2\kappa_1+6}{3}\mu + (\kappa_1 - 3)\mu^V & \frac{4b^2\kappa_1-6}{3b^2}\mu + (\kappa_1 - 3)\mu^V & \frac{4a^2\kappa_1-6}{3a^2}\mu + (\kappa_1 - 3)\mu^V \\ \frac{2\kappa_2}{3}\mu - \kappa_2\mu^V & -\frac{a^2+2b^2}{a^2b^2}\mu - \kappa_2\mu^V & \frac{2a^2+b^2}{a^2b^2}\mu - \kappa_2\mu^V \end{bmatrix}, \tag{28}$$

where $\kappa_1 = 1/a^2 + 1/b^2 + 1, \kappa_2 = 1/a^2 - 1/b^2$. The notation g_{ij} is introduced here only because otherwise the expressions for h_{ij} would be too long to be written within a line. We find that h_{ij} are functions of the aspect ratios a and b, shear and bulk viscosities μ and μ^V, relaxation parameters s_e, and s_n, sound speed c_s, and γ. The expressions for h_{ij} are derived based on the requirements in Eq. (22) and they work together to achieve two goals:

1. There could be three shear viscosity coefficients and three bulk viscosity coefficients in Eq. (22a)(22b)(22c) and these viscosity coefficients would be different in different directions if we set $h_{ij} = 0$, as shown clearly in [10] for some 2D rectangular-grid models. Thus, h_{ij} are used to achieve the isotropy conditions, namely, all shear viscosity coefficients are constrained to a same value, and all bulk viscosity coefficients are made identical. This was our original motivation of extending the equilibrium moments as in Eq. (7b).

2. After the key model parameters, a, b, μ, μ^V, s_e, s_n, c_s, and γ are chosen, we can always find a solution for h_{ij} such that Eq. (22) holds true and shear (and bulk) viscosity are consistent in different equations.

2.3. Summary of the proposed D3Q19 model on a cuboid grid

We shall now summarize the derived model details that are needed to implement the model. First, the equilibrium moments at both the leading order and the next order are summarized as

$$\mathbf{m}^{(eq)} = \begin{bmatrix} \delta\rho \\ 19\delta\rho\left(c_s^2 + \frac{c_s^2}{a^2} + \frac{c_s^2}{b^2} - \frac{30}{19}c^2\right) + 19\rho_0\left(u^2 + \frac{v^2}{a^2} + \frac{w^2}{b^2}\right), \\ \varepsilon^{(eq,0)} \\ \rho_0 u \\ \gamma c^2 \rho_0 u \\ \rho_0 v/a \\ \frac{a^2\kappa_3 - 4}{a} c^2 \rho_0 v \\ \rho_0 w/b \\ \frac{b^2\kappa_3 - 4}{b} c^2 \rho_0 w \\ \delta\rho\left(2c_s^2 - \frac{c_s^2}{a^2} - \frac{c_s^2}{b^2}\right) + \rho_0\left(2u^2 - \frac{v^2}{a^2} - \frac{w^2}{b^2}\right) \\ \pi_{xx}^{(eq,0)} \\ \delta\rho c_s^2 \frac{b^2 - a^2}{a^2 b^2} + \rho_0\left(\frac{v^2}{a^2} - \frac{w^2}{b^2}\right) \\ \pi_{ww}^{(eq,0)} \\ \rho_0 uv/a \\ \rho_0 uw/b \\ \rho_0 vw/ab \\ 0 \\ 0 \\ 0 \end{bmatrix} + \rho_0\delta_t c^2 \begin{bmatrix} 0 \\ h_{11}\partial_x u + h_{12}\partial_y v + h_{13}\partial_z w \\ 0 \\ 0 \\ 0 \\ 0 \\ 0 \\ 0 \\ 0 \\ h_{21}\partial_x u + h_{22}\partial_y v + h_{23}\partial_z w \\ 0 \\ h_{31}\partial_x u + h_{32}\partial_y v + h_{33}\partial_z w \\ 0 \\ \lambda\left(\partial_y u + \partial_x v\right)/a \\ \left[0.1 s_c^* \kappa_3\left(a^2 b^2 - a^2\right) + \lambda\right]\left(\partial_z v + \partial_y w\right)/(ab) \\ \left[0.1 s_c^* \kappa_3\left(b^2 - a^2\right) + \lambda\right]\left(\partial_x w + \partial_z u\right)/b \\ 0 \\ 0 \\ 0 \end{bmatrix}, \tag{29}$$

$$\epsilon j_x^{(1)} = -F_x\delta_t/2, \;\; \epsilon j_y^{(1)} = -F_y\delta_t/2a, \;\; \epsilon j_z^{(1)} = -F_y\delta_t/2b, \tag{30}$$

where the first array on the right represents the equilibrium moments at the leading order $\mathbf{m}^{(eq,0)}$ and the second array on the right represents the equilibrium moments at the next order $\mathbf{m}^{(eq,1)}$, namely, the extended equilibrium moments. As before, $\kappa_3 = (\gamma + 4)$, $s_e^* = (2 - s_e)/2s_e$, $s_n^* = (2 - s_n)/2s_n$, $s_c^* = (2 - s_c)/2s_c$. The essential key adjustable parameters are γ, λ, h_{ij} and c_s^2. The coefficients h_{ij} are defined by Eq. (27) and (28). Furthermore, $\varepsilon^{(eq,0)}, \pi_{xx}^{(eq,0)}$ and $\pi_{ww}^{(eq,0)}$ are not constrained by the N-S equations, therefore, theoretically they can be set to any value. Usually we choose $\varepsilon^{(eq,0)} = \alpha c^4\delta\rho + \beta\rho_0 c^2\left(u^2 + v^2\right), \pi_{xx}^{(eq,0)} = \omega_{xx} c^2 p_{xx}^{(eq,0)}, \pi_{ww}^{(eq,0)} = \omega_{ww} c^2 p_{ww}^{(eq,0)}$, where the values of $\alpha, \beta, \omega_{xx}, \omega_{ww}$ could be determined through a linear stability analysis [23, 24]. Other extended equilibrium moments and forcing terms in Eq. (29) that are not constrained by the N-S equations are simply set to zero for simplicity. The potential use of these terms as a way to optimize numerical stability of the current model can be a topic of investigation in the future.

It is also important to note that the cuboid model would reduce to the standard D3Q19 MRT LBM indicated in [23] when both aspect ratios a and b are set to 1, and the equilibrium moments are not extended, namely, $h_{ij} = \lambda = 0$. Also, the exact definitions of all equilibrium moments in [23] could be recovered from Eq. (29).

Our derivation shows that $m_1^{(1)} = \Psi_1^{(1)} = 0$, thus the presence of forcing does not affect the local density fluctuation and the calculation of pressure is not affected. Also, according to the multi-scale expansion in Eq. (7a), $m_4 = j_x^{(0)} + \epsilon j_x^{(1)} = \rho_0 u - F_x\delta_t/2$. Therefore, the computation of hydrodynamic velocity is affected by the forcing, *i.e.,* $\rho_0 u =$

$\mathbf{M}_{4i} f_i + F_x \delta_t/2$. The same applies to the velocity in the y and z direction. Thus, the pressure and velocity in this model should be calculated according to

$$p = \delta\rho c_s^2, \tag{31a}$$

$$u = \left(\mathbf{M}_{4i} f_i + F_x \delta_t/2\right)/\rho_0, \tag{31b}$$

$$v = \left(a\mathbf{M}_{6i} f_i + F_y \delta_t/2\right)/\rho_0, \tag{31c}$$

$$w = \left(b\mathbf{M}_{8i} f_i + F_z \delta_t/2\right)/\rho_0. \tag{31d}$$

Putting all the above results together for the forcing term, we have

$$\mathbf{\Psi} = \epsilon\mathbf{\Psi}^{(1)} = \begin{bmatrix} 0 \\ 38(1-0.5s_e)(uF_x + vF_y/a^2 + wF_z/b^2) \\ \Psi_3 \\ (1-0.5s_j)F_x \\ \Psi_5 \\ (1-0.5s_j)F_y/a \\ \Psi_7 \\ (1-0.5s_j)F_z/b \\ \Psi_9 \\ 2(1-0.5s_n)(2uF_x - vF_y/a^2 - wF_z/b^2) \\ \Psi_{11} \\ 2(1-0.5s_n)(vF_y/a^2 - wF_z/b^2) \\ \Psi_{13} \\ (1-0.5s_c)(vF_x + uF_y)/a \\ (1-0.5s_c)(vF_x + uF_y)/ab \\ (1-0.5s_c)(vF_x + uF_y)/b \\ \Psi_{17} \\ \Psi_{18} \\ \Psi_{19} \end{bmatrix}. \tag{32}$$

A few observations about the mesoscopic forcing term can now be made: (1) The components of the mesoscopic forcing term are related to macroscopic forcing field $\mathbf{F} = \left(F_x, F_y, F_z\right)$, macroscopic velocity, and relaxation parameters. The mesoscopic forcing terms $\mathbf{\Psi}$ are added to Eq. (2) as $\mathbf{\Phi} = \mathbf{M}^{-1}\mathbf{\Psi}\delta_t$ to realize the effect of macroscopic forcing at the mesoscopic level; (2) nine of the 19 components: Ψ_3, Ψ_5, Ψ_7, Ψ_9, Ψ_{11}, Ψ_{13}, Ψ_{17}, Ψ_{18}, and Ψ_{19}, are not constrained by the N-S equations and thus they can be specified *freely*. Basically, only the components associated with the 0^{th}, 1^{st}, and 2^{nd} order moments are determined by the continuity and N-S equations. In principle, we could manipulate the nine irrelevant components in the forcing term, to further enhance numerical stability.

The above completes the description of the MRT LBM model details on a cuboid lattice, with a general nonuniform forcing. We should now provide a few general comments on how to use this model in a typical application of solving a 3D viscous flow. First, all physical parameters of a flow problem are gathered, namely, viscosity coefficients μ and μ^V, macroscopic forcing field $\mathbf{F}$, domain size, the initial condition, boundary conditions of the flow, *etc*. They determine the length scale L, characteristic velocity U_0, and the flow Reynolds number. Next, key parameters of the cuboid model and numerical settings are specified, including grid aspect ratios a and b, speed of sound c_s, the coefficient in the $x-$component energy flux γ, relaxation parameters $\mathbf{S}$. In the proposed cuboid model, in principle, the relaxation parameters can be set to any value between 0 and 2 as long as the code is stable, because enough degrees of freedom are introduced so the relaxation parameters are not uniquely related to the physical viscosity coefficients. The parameter λ is then calculated according to Eq. (26a). With Eqs. (27) and (28), h_{ij} are then determined from μ, μ^V, a, b, c_s, relaxation parameters, and γ. Thus, all equilibrium moments $\mathbf{m}^{(eq)}$ can now be specified using Eq.

(29). The mesoscopic forcing term $\mathbf{\Psi}$ is also known from Eq. (32). Therefore, we could advance the flow step by step according to the lattice Boltzmann equation, Eq. (2). In the cuboid model, the additional equilibrium moments $\epsilon\mathbf{m}^{(eq,1)}$ contain strain-rate components. Thus, we need to compute them every time step. These strain-rate components can be calculated from the non-equilibrium moments so they all have a second-order accuracy. The method of calculating strain-rate components is given in the Appendix.

3. Numerical validations

In this section, the D3Q19 MRT lattice Boltzmann method on a cuboid lattice grid derived in Sec. 2 will be validated with three different benchmark cases: the transient laminar channel flow, the three-dimensional decaying Taylor-Green vortex flow, and the turbulent channel flow. Furthermore, the order of numerical accuracy of this model will be examined.

3.1. The laminar channel flow

First, we use the two-dimensional, transient, laminar channel flow to validate the cuboid model as the analytical solution for this time-dependent flow is available. The laminar channel flow is a wall-bounded flow with two parallel flat walls. In the simulation, the mid-link bounce back scheme is applied to fulfill the no-slip boundary condition. The wall boundary is placed half lattice away from the boundary fluid nodes. On each link cutting the wall, the inward post-streaming non-equilibrium distribution of a boundary node is set to the pre-streaming distribution in the opposite direction, namely, $f_{\bar{i}}(\mathbf{x}_B, t+\delta_t) = \tilde{f}_i(\mathbf{x}_B, t)$ where $\mathbf{x}_B$ is the location of a boundary node, $\tilde{f}_i$ represents the post-collision (pre-streaming) distribution function with particle velocity e_i, which points into the wall. $f_{\bar{i}}$ represents the post-streaming distribution function in the direction opposite to e_i.

The domain is three-dimensional, with periodic boundary conditions in both the streamwise and the spanwise directions. In the code, x, y, and z represent the transverse, streamwise, and spanwise direction, respectively. All simulation results from the cuboid D3Q19 model are compared to the analytical solution.

In Table 1, the parameter settings of the cuboid model with four different aspect ratios are listed. In the most extreme case, the aspect ratio $a = \delta_y/\delta_x = \delta_{streamwise}/\delta_{transverse}$ and $b = \delta_z/\delta_x = \delta_{spanwise}/\delta_{transverse}$ are set to 20, thus the lattice in this case looks like a square plate. The channel height H of all cases is set to $H = 40\delta_{transverse}$. Since the flow is laminar, there is no variation in *streamwise* and *spanwise* directions. We only need to resolve the flow in the *transverse* direction and in time. The computational domain size for all cases is set to $N_x \times N_y \times N_z = 40 \times 2 \times 2$. The maximum streamwise velocity V_{max} is set to 0.1 and the speed of sound c_s is set to 0.6325 so the maximum Mach number is much smaller than 1/3. The kinematic shear and bulk viscosities are set to 0.1333 so the steady-state Reynolds number $Re = V_{max}H/\nu$ is 30. The adjustable parameter γ depends on the aspect ratio as this parameter was found to affects the numerical stability of the cuboid model. For all cases, all relaxation parameters in Eq. (5) are set to 1.2.

The flow starts from rest, and a uniform and constant body force F_y $[kg \cdot m^{-2} \cdot s^{-2}]$ is applied in the streamwise direction to drive the flow to its steady state with the long-time maximum velocity V_{max} at the channel centerline. The external body force F_y according to the steady-state solution is

$$F_y = \frac{8\rho_0 \nu V_{max}}{H^2}. \tag{33}$$

In Fig. 2(a), the time evolution of the streamwise velocity v at $x/H = 0.4875$ is shown for all cases. The theoretical velocity at this location is also plotted as the benchmark. Under the constant uniform external force, the streamwise velocity increases with time. The steady-state velocity is reached at roughly $t\nu/H^2 = 0.5$, when the the external force is balanced by the viscous shear stress. Since the location we selected is $x/H = 0.4875$, which is very close to the center of channel, the ratio v/V_{max} at the steady state is very close to one. Results from all aspect ratios are in excellent agreement with the theory at all times.

In Figs. 2(b) and 2(c), the streamwise velocity profiles and the profiles of velocity gradient dv/dx are shown, respectively. There are six different curves in the plots and they represent the profiles at six different times: $t\nu/H^2 = 0, 0.025, 0.0541, 0.0967, 0.167, 1.25$, respectively. All results are compared to the theoretical velocity profiles at the corresponding time and again an excellent agreement is observed, regardless of the aspect ratios used.

Table 1: Parameter settings of the laminar channel flow with cuboid lattice grids.

Cases	Aspect ratio	H	V_{max}	ν	ν^V	c_s	γ	Re
1	$a = b = 2$	40	0.1	0.1333	0.1333	0.6325	−3.0	30
2	$a = b = 4$	40	0.1	0.1333	0.1333	0.6325	−3.8	30
3	$a = b = 10$	40	0.1	0.1333	0.1333	0.6325	−3.97	30
4	$a = b = 20$	40	0.1	0.1333	0.1333	0.6325	−3.98	30

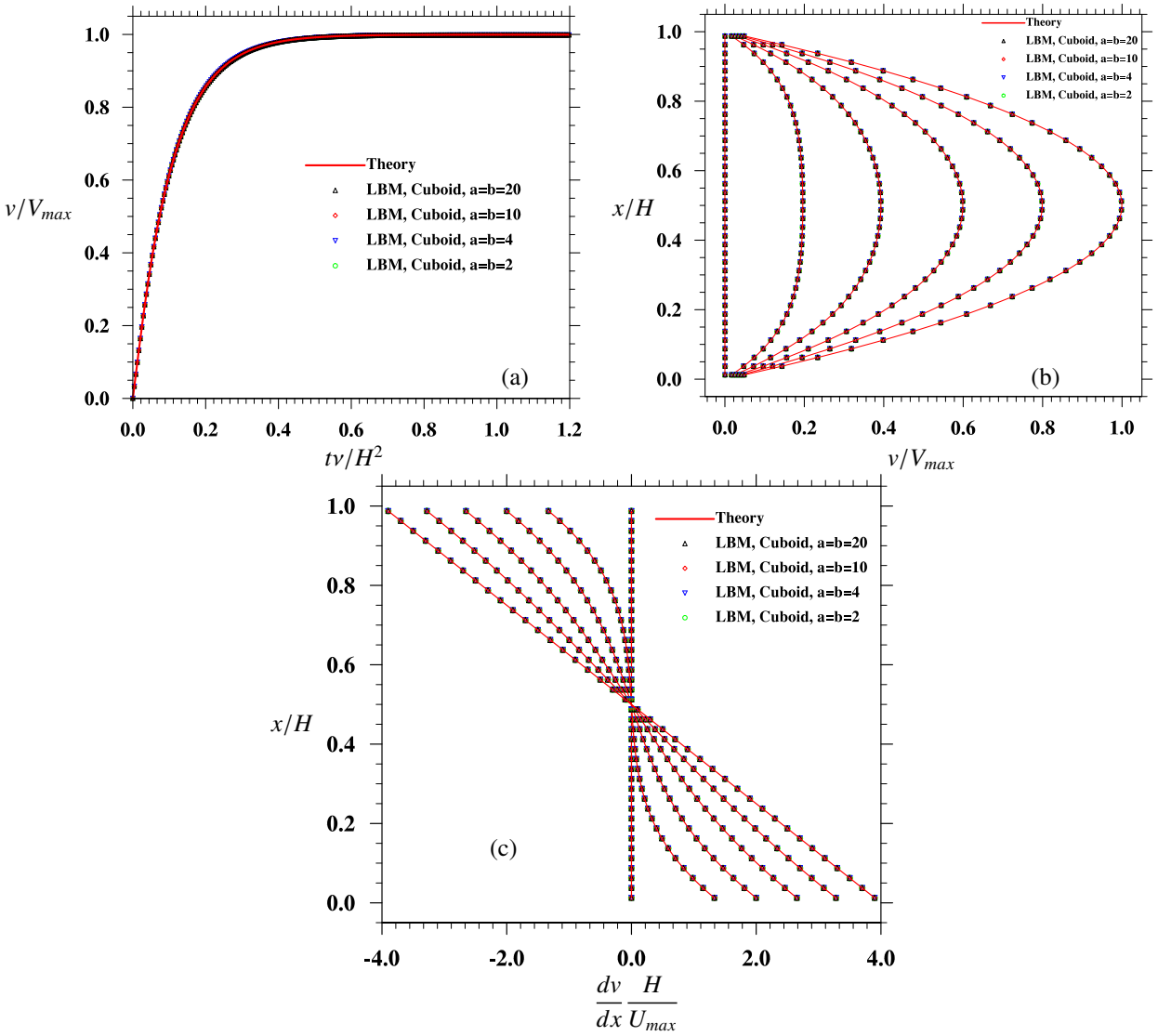

Figure 2: (a) The time evolution of the streamwise velocity v at $x/H = 0.4875$ (close to the channel centerline). (b) The streamwise velocity profiles and (c) the profiles of velocity gradient dv/dx at six different times, $t\nu/H^2 = 0, 0.025, 0.0541, 0.0967, 0.167$, and 1.25, All quantities are normalized as indicated.

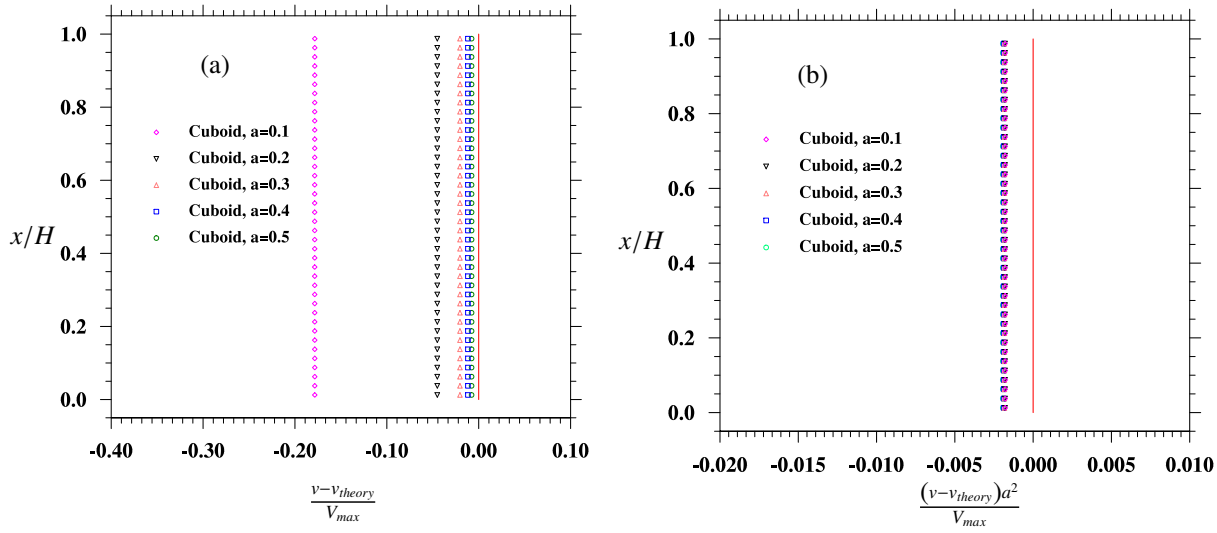

Figure 3: (a) The numerical error profiles of different aspect ratios at the steady state ($t\nu/H^2 = 1.25$). (b) The rescaled normalized numerical error profiles ($t\nu/H^2 = 1.25$). Here $H = 40$, and all quantities are normalized as indicated.

Recall that the original goal of developing the cuboid lattice model is to improve the efficiency of LBM simulations, especially for wall-bounded flows. Therefore, in previous tests on the laminar channel flow, the streamwise direction (the direction of main flow) is aligned on the wider lattice spacing side of cuboid lattice ($a = \delta_y/\delta_x > 1$). For completeness, we next investigate the situation when the main flow velocity is aligned with the shorter lattice side ($a = \delta_y/\delta_x < 1$). The second aspect ratio $b = \delta_z/\delta_x$ is fixed to one as the lattice spacing in the z direction is essentially irrelevant for the 2D laminar flow. As shown in Table 2, five cases are tested with the aspect ratio a as the only variable and $a < 1$ so that the shorter lattice side is parallel to the streamwise direction. In previous tests with aspect ratios $a, b > 1$, the smallest lattice spacing is $\delta_x = 1$. Now, the smallest lattice spacing becomes $\delta_y = a < 1$ in lattice units. Since the lattice spacing is the product of molecule discrete velocity and time step, the speed of sound should be reduced accordingly, to accommodate the smaller minimum lattice spacing, as recognized in Peng *et al.* [16]. Consequently, the flow velocity should be reduced proportionally to maintain a small Mach number, so is the Reynolds number.

As shown in He *et al.* [21], LBM yields a constant numerical error (*i.e.*, independent of the wall-normal location) for the case of steady-state laminar channel flow. This error could be determined analytically and it is related to the relaxation parameter and the number of lattice grids in the wall-normal direction[21]. In Fig. 3(a) the numerical error profiles at steady state are plotted for the five cases with different aspect ratios . It is shown that the error is also independent of the wall normal location, with its magnitude increasing with decreasing aspect ratio. In Fig. 3(b) the same numerical error is further rescaled by multiplying it by a^2. The error data collapse, implying that the numerical error scales with $1/a^2$. Furthermore, it is found that the numerical error varies with the coefficient γ involved in the equilibrium energy flux, but the effect of aspect ratio dominates the resulting error. Thus, a large numerical error would occur when a small aspect ratio is applied. In this case, one way to ensure the numerical accuracy is to increase the grid resolution in the wall normal direction. The fact that the numerical solution converges to the theoretical value again shows that our cuboid model is physically correct. Although this is computationally more expensive but it does not contradict with our motivation since we usually align the large-velocity direction with the wider lattice side so the aspect ratio δ_y/δ_x is usually larger than one.

In Fig. 4, the numerical results using 200 lattices in the wall normal direction are shown (all other parameters are the same as Case 2 in Table 2). The results are in excellent agreement with the theory as the numerical error is small according to Fig. 4(b).

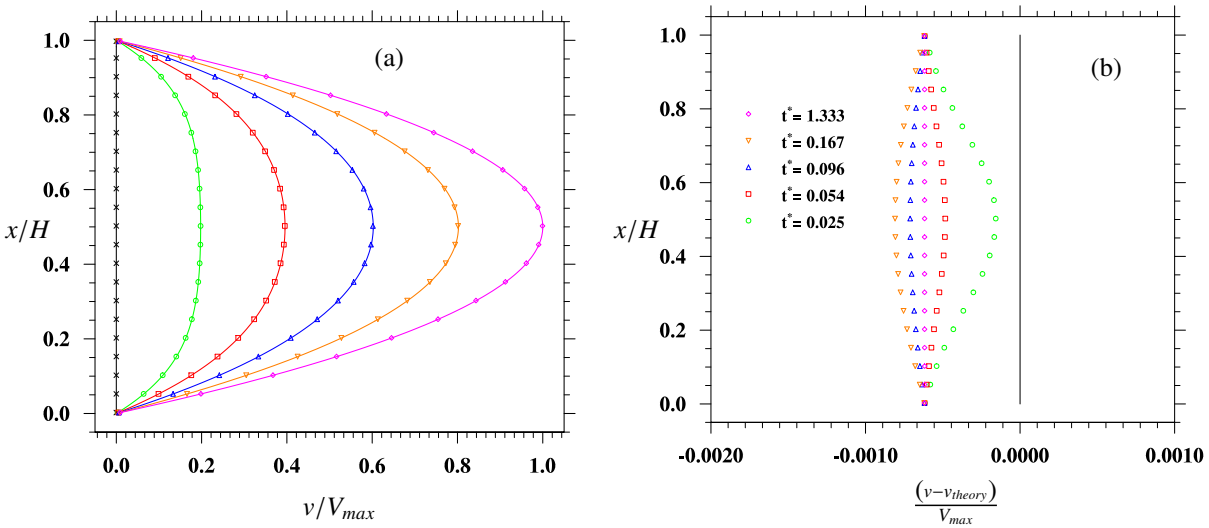

Figure 4: (a) The streamwise velocity profiles at at different times $t\nu/H^2 = 0.025, 0.0541, 0.0967, 0.167, 1.25$ obtained with $H = 200$. (b) The numerical error profiles at at different times $t\nu/H^2 = 0.025, 0.0541, 0.0967, 0.167, 1.25$ obtained with $H = 200$. All quantities are normalized as indicated.

Table 2: Parameter settings of the laminar channel flow when the aspect ratio a is smaller than one. The streamwise direction is aligned with the shorter lattice side of the cuboid grid.

Cases	Aspect ratio	H	V_{max}	ν	ν^V	c_s	γ
1	$a = 0.1, b = 1$	40	0.005	0.1333	0.1333	0.1	−3.5
2	$a = 0.2, b = 1$	40	0.005	0.1333	0.1333	0.1	−3.5
3	$a = 0.3, b = 1$	40	0.005	0.1333	0.1333	0.1	−3.5
4	$a = 0.4, b = 1$	40	0.005	0.1333	0.1333	0.1	−3.5
5	$a = 0.5, b = 1$	40	0.005	0.1333	0.1333	0.1	−3.5

Table 3: Parameter settings of the 3D decaying Taylor-Green vortex flow.

Cases	Aspect ratio	L	$N_x \times N_y \times N_z$	Re_0	U_0	ν	ν^V	c_s^2	γ
1	$a = b = 0.8$	64	$64 \times 80 \times 80$	300	0.10186	0.0035	0.0035	0.3	−1.5
2	$a = b = 0.8$	128	$128 \times 160 \times 160$	300	0.05093	0.0035	0.0035	0.3	−2.0
3	$a = b = 0.5$	64	$64 \times 128 \times 128$	30	0.05	0.0017	0.0017	0.08	−0.2

3.2. The 3D Taylor-Green vortex flow

The 3D Taylor-Green vortex flow was proposed by Taylor and Green [22] to study the production of small eddies from large eddies. They solved the three-dimensional time-dependent flow analytically using a short-time perturbation expansion, making this an ideal benchmark for any 3D numerical method. In the 3D Taylor-Green flow, the kinetic energy of the flow decreases in time, and at the same time, is transferred from the initial large-scale eddy to newly-created small-scale eddies. The energy-cascading feature is not present in the 2-D Taylor-Green vortex flow [10] often used to validate numerical methods in 2D. We have also solved the 3D Taylor-Green vortex flow by a highly-accurate pseudo-spectral method. Both the short-time analytical solution and the spectral solution will be used to validate the present cuboid-lattice model.

Specifically, we consider the 3D Taylor-Green vortex flow with the following initial velocity field

$$\begin{cases} u = U_0 cos\,(2\pi x/L)\, sin\,(2\pi y/L)\, sin\,(2\pi z/L)\,, \\ v = -U_0 sin\,(2\pi x/L)\, cos\,(2\pi y/L)\, sin\,(2\pi z/L)\,, \\ w = 0, \end{cases} \tag{34}$$

where u, v and w represent the velocity in the x, y, z directions, respectively. U_0 is the characteristic velocity of the flow at the initial time. The domain size is L, which is the same in the three directions. Periodic boundary condition is assumed in all three directions.

Taylor and Green [22] obtained the short-time perturbation solution as follows. First, a Poisson equation of the pressure could be derived by combining the continuity equation with the N-S equations. Based on the initial velocity given in Eq. (34), the pressure field could be solved from the Poisson equation. Next, the pressure is then substituted back to the N-S equations to determine the time derivative of velocity at the initial time, which can be integrated to obtain the first approximation of the short-time solution. The above process (velocity - pressure - time derivative of velocity - new velocity) is regarded as one perturbation iteration. Then, the new velocity field becomes the starting solution for the next iteration. After a few iterations, the short-time theoretical solution of the 3D Taylor-Green vortex flow can be obtained, with the time dependence expressed through mode coefficients as polynomials in time. The final three-dimensional time-dependent perturbation solution of the velocity field, the average kinetic energy, and the average dissipation rate are presented in [22].

Some key parameter settings of this flow are listed in Table 3. We first tested two cases with an aspect ratio $a = \delta_y/\delta_x = 0.8$ and $b = \delta_z/\delta_x = 0.8$. The domain size L is set to $L_x = L_y = L_z = 64$ and 128, respectively. The number of lattices in each direction is chosen according to the aspect ratio $a = \delta_y/\delta_x$ and $b = \delta_z/\delta_x$ to keep the physical domain size identical. Since the flow is decaying, Re_0 represents the initial Reynolds number defined as $Re_0 = (U_0 L)\,/\,(2\pi\nu)$. The relaxation parameter of both cases are set to $s_e = 0.8, s_\varepsilon = 0.6, s_q = 0.8, s_n = 0.8, s_c = 0.8, s_\pi = 0.8, s_m = 1.95$ to obtain a better stability. In the first two cases, results of the cuboid model are compared with results of the corresponding MRT-LBM with cubic lattice and spectral method.

Four statistics of the flow are calculated and compared to the results of other models and the short-time theory, the average kinetic energy $E = \langle \mathbf{u}_i^2 \rangle/2$, averaged total dissipation rate $D = 2\nu\langle \left(S_{ij} - \nabla\cdot\mathbf{u}\delta_{ij}/3\right)^2 + \nu^V (\nabla\cdot\mathbf{u})^2 \rangle$, where S_{ij} is the strain rate, ν^V is the bulk viscosity and $\nabla\cdot\mathbf{u}$ is the divergence. The effect of bulk viscosity is considered since the usual LBM simulation is not fully incompressible so the divergence of the flow is not strictly zero. If the flow is fully incompressible, then the total dissipation rate would reduce to $D = 2\nu\langle S_{ij}^2 \rangle$. The velocity skewness $S_{\mathbf{u}}$ and flatness $F_{\mathbf{u}}$

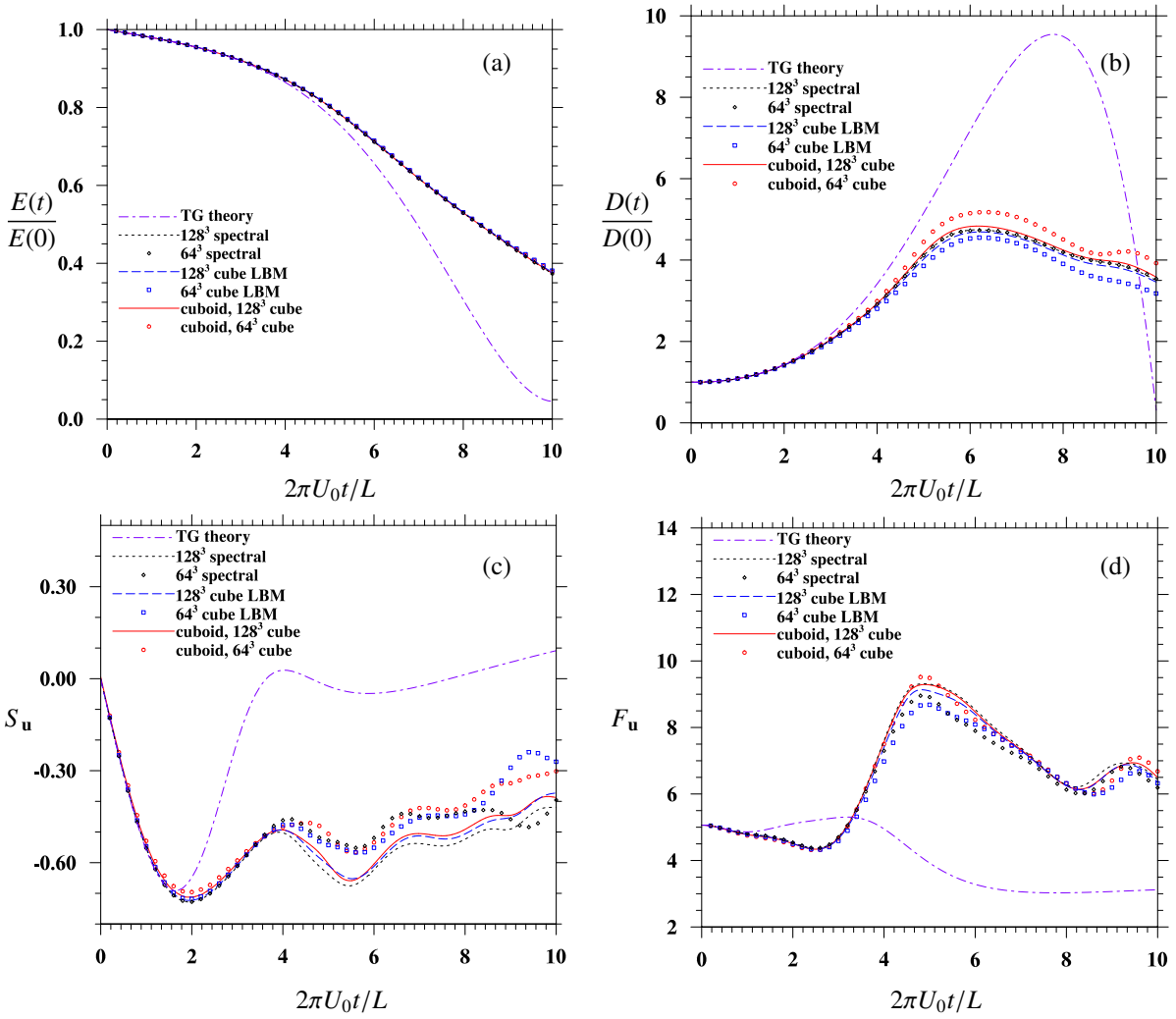

Figure 5: The time evolutions of (a) the average kinetic energy E_k, (b) the average dissipation rate ϵ, (c) the velocity-derivative skewness, and (d) the velocity-derivative flatness. The results of two cuboid cases in Table 3 are compared to those of the two MRT-LBM cases with the cubic lattice and two different resolutions, the spectral method, and the short-time theory .

are calculated. The velocity skewness and flatness are defined as

$$S_{\mathbf{u}} = \frac{\left\langle \frac{1}{3}\left[(\partial_x u)^3 + \left(\partial_y v\right)^3 + (\partial_z w)^3\right]\right\rangle}{\left\langle \frac{1}{3}\left[(\partial_x u)^2 + \left(\partial_y v\right)^2 + (\partial_z w)^2\right]\right\rangle^{3/2}}, \tag{35a}$$

$$F_{\mathbf{u}} = \frac{\left\langle \frac{1}{3}\left[(\partial_x u)^4 + \left(\partial_y v\right)^4 + (\partial_z w)^4\right]\right\rangle}{\left\langle \frac{1}{3}\left[(\partial_x u)^2 + \left(\partial_y v\right)^2 + (\partial_z w)^2\right]\right\rangle^{2}}, \tag{35b}$$

where S_u and F_u represent the velocity skewness and flatness, respectively. The velocity skewness and flatness are high order statistics and thus could be used to evaluate the accuracy of the small scale structure of the simulation.

In Fig. 5, the results of two cuboid cases are compared to the corresponding MRT-LBM with cubic lattice, and spectral method, and the theoretical solution of 3D Taylor-Green vortex flow. The 128^3 spectral method is the most accurate one because LBM is a second-order accurate method and the order of accuracy of the spectral method is

higher than two. In Fig. 5, all curves are matched at the beginning, including the short-time theory of the Taylor-Green vortex flow. But the theoretical solutions of 3D Taylor-Green vortex flow are only valid for a short time. For low order statistics like kinetic energy and dissipation rate, the short-time theory is valid for about 2 non-dimensional time. For higher order statistics like velocity skewness, the theory of 3D Taylor-Green vortex flow is valid for about 1.5 non-dimensional time and the lifetime of theoretical velocity flatness is less than 1.

In Fig. 5(a), the kinetic energy decays monotonically. The time evolution of normalized kinetic energy of all models are matched with a good agreement, which means the large structure is adequately captured by all models with two different resolutions. Meanwhile, the result of high resolution cases is slightly better than low resolution cases comparing to the 128^3 spectral method, which is expected. Fig. 5(b) shows the time evolution of the normalized dissipation rate of the flow. The results from all models are identical until two non-dimensional times, which is expected since all simulations are initialized with the same profile and there are only large flow structures in the initial field so the flow is well resolved at the beginning of all cases. As indicated in [22], small-scale flow structure like small eddies will be created from large eddies. Therefore, to fully resolve the flow, the number of lattice grids should also be increased. For a quantity like dissipation rate which is related to the small-scale structure of the flow, it is easy to tell that the result of 128^3 cubic and cuboid LBM is much better than the corresponding 64^3 cases. Different from the evolution of kinetic energy, the dissipation of the flow first increases due to the production of small-scale structure and then decreases since the flow is decaying and the Reynolds number is reducing.

Fig. 5(c)(d) shows the time evolution of the velocity-derivative skewness and flatness of different models. Recall that in Fig. 5(b), the difference of kinetic energy between different resolutions are small. Here we observe that all high resolution cases are significantly better than low resolution cases comparing to the 128^3 spectral method. This is because the velocity-derivative skewness and flatness are high-order quantities and are more sensitive to the fluid motion at small scales. The above results mean that 64^3 is not enough to fully resolve the flow. Another reason of the discrepancy between different models is that the system is highly non-linear. Therefore, a small error would increases rapidly over time and leads to a different local structure. If the time of simulation is long enough, even the whole domain would be affected by the difference of local flow structures. For example, the results of two spectral simulations at different resolutions are only matched till 3.5 non-dimensional times. Therefore, results of the proposed cuboid lattice model are still reasonable comparing to the spectral method and the LB models with cubic lattice.

In Fig. 6, the velocity profiles on the line $x/L = 1/4, y = z$, at the non-dimensional time $2\pi U_0 t/L = 5$, is plotted for the cuboid case 1 in Table 3 and a MRT-LBM with 64^3 cubic lattices. The velocity profiles of two models are matched exactly. The velocity profiles at other times and on some other lines are also examined (but not shown here), and in all cases the results of the cuboid model are in excellent agreement with MRT-LBM results with a cubic lattice.

In the 3D Taylor-Green vortex flow at $Re_0 = 300$, due to the strong non-linearity and local anisotropy of flow, the capability of the proposed cuboid lattice model is limited due to the lack of numerical stability when lattice aspect ratio is reduced below 0.8. However, we are able to simulate the same flow at $Re_0 = (U_0 L) / (2\pi\nu) = 30$ with an aspect ratio of $a = b = 0.5$. The parameter setting of this case is given in case 3 of Table 3. The code remains stable and the results are in good agreement with the benchmark data from MRT-LBM on cubic lattice grid, as shown in Fig. 7. Therefore, 0.8 is not the lower limit of the aspect ratio, although the origin for numerical instability for the case of high Re_0 and lower aspect ratios requires further investigation.

3.3. Order of accuracy

It has been known that the lattice Boltzmann method has a second-order accuracy in space and time [10, 16, 28]. The order of accuracy of the proposed cuboid model can be examined using the results for the transient laminar channel flow and the 3D decaying Taylor-Green vortex flow presented in Sec. 3.1 and 3.2. To examine the accuracy with the laminar channel flow, we use Case 2 in Table 1 ($a = b = 4$) with four different grid resolutions: $10 \times 2 \times 2, 20 \times 4 \times 4, 40 \times 8 \times 8$, and $80 \times 16 \times 16$. Other parameters are the same as in Table 1 and all results are compared to the theoretical solution. To study the accuracy with 3D Taylor-Green vortex flow, we choose Case 1 in Table 3 (a = b = 0.8) with 5 different resolutions: $32 \times 40 \times 40, 64 \times 80 \times 80, 128 \times 160 \times 160, 256 \times 320 \times 320$, and $512 \times 640 \times 640$. Due to the anisotropy of lattice sizes of the cuboid model, it is impossible to match the node points in the cuboid model with other models like the spectral method based on the cubic grid. The short-time theory of 3D Taylor-Green flow could be a great benchmark tool for average statistics like the average kinetic energy, but it is only valid at short times. However, the order of accuracy must be based on local errors at the exact same locations. Therefore, we instead use the results of the cuboid model at $512 \times 640 \times 640$ as the benchmark when computing local errors for the other 4

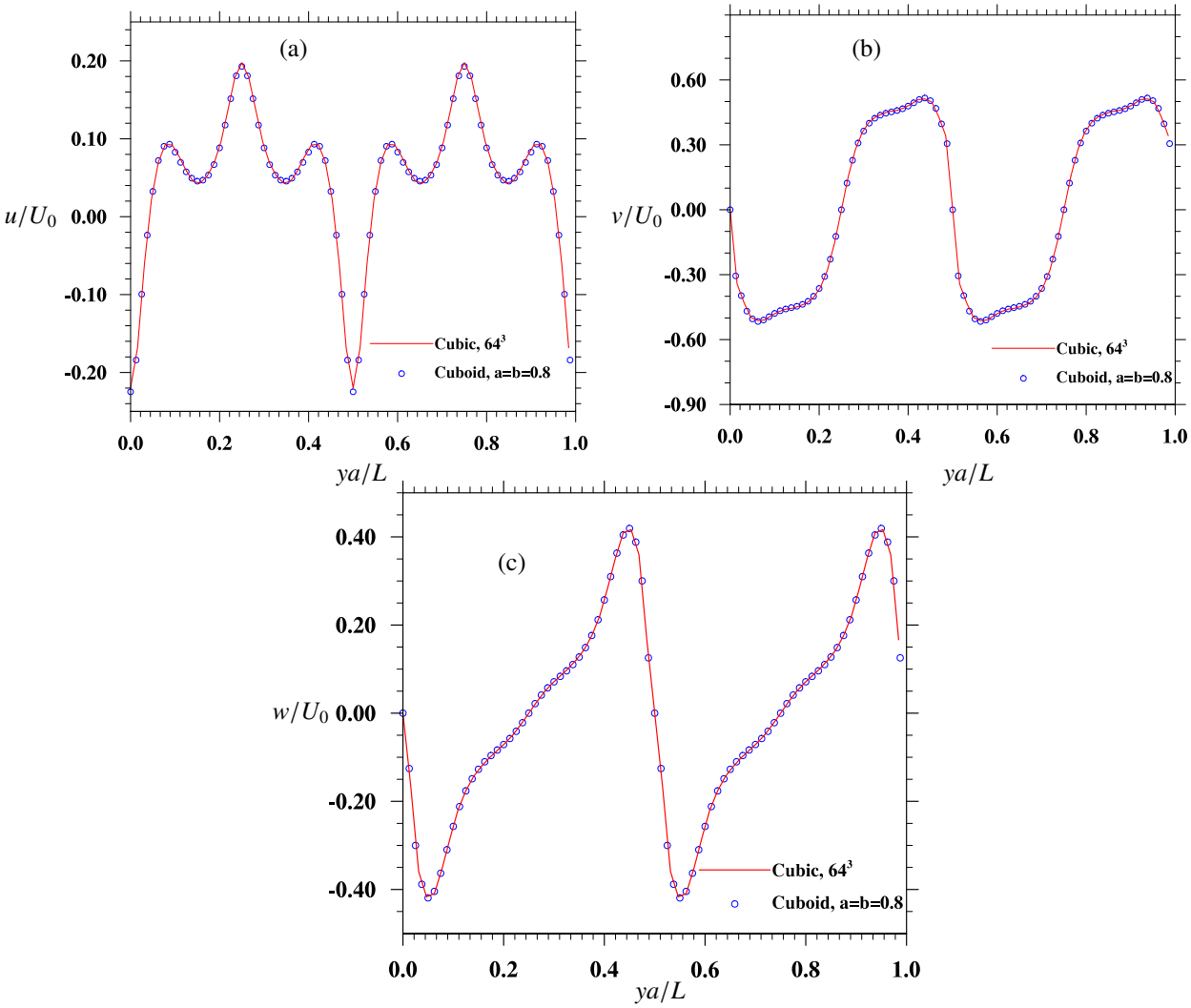

Figure 6: The velocity profiles on a line $x/L = 1/4$ and $y = z$ at the non-dimensional time $2\pi U_0 t/L = 5$. (a) Velocity in the x direction, (b) velocity in the y direction, and (c) velocity in the z direction. Results of the cuboid model are compared to results of the corresponding MRT-LBM with 64^3 cubic lattice. All quantities are normalized as indicated.

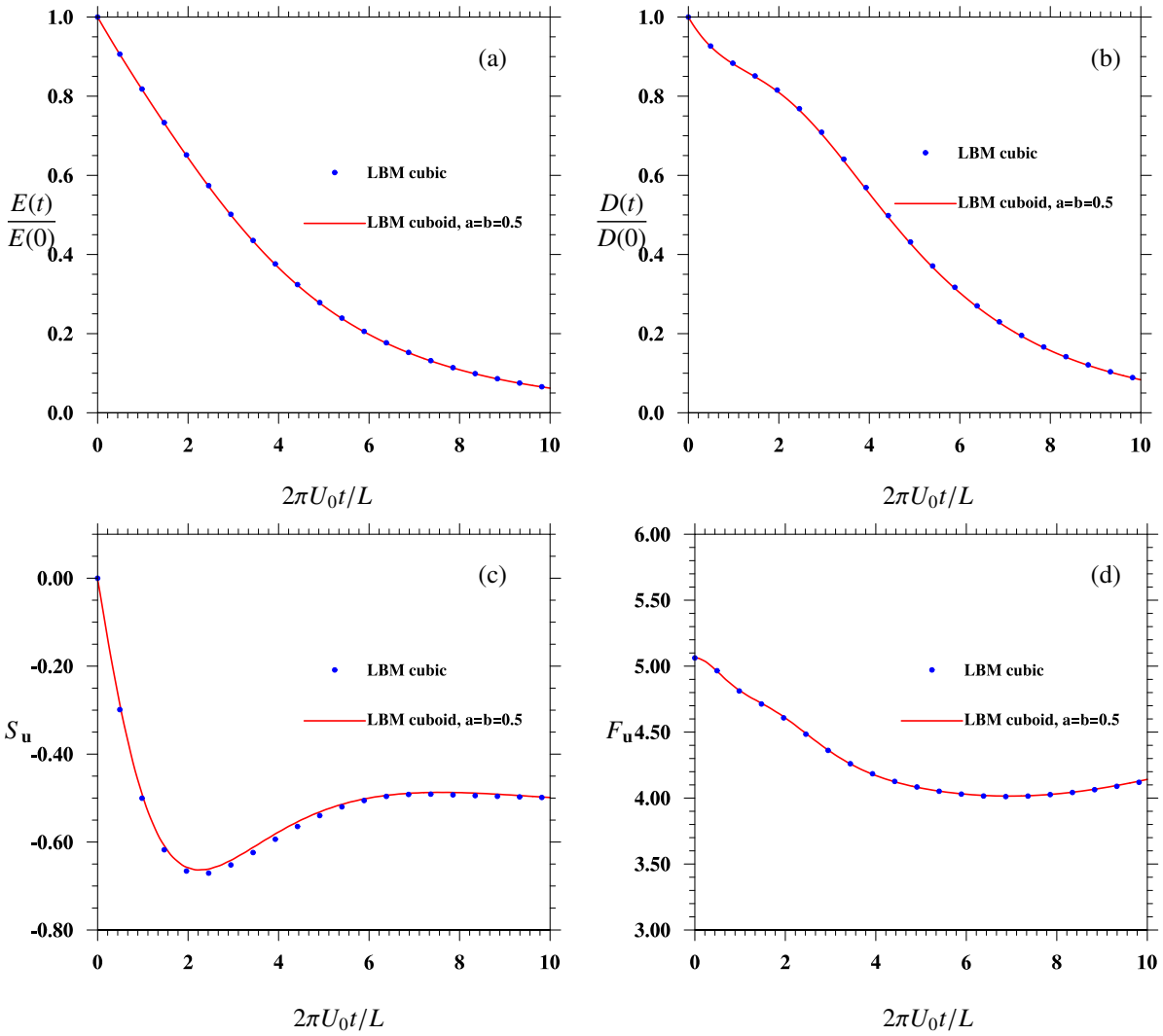

Figure 7: The time evolutions of (a) the kinetic energy E_k, (b) the total dissipation rate ϵ, (c) the velocity-derivative skewness, and (d) the velocity-derivative flatness. Results of the cuboid model at $Re_0 = 30$ with $a = b = 0.5$ are compared to the MRT-LBM on cubic lattices.

Table 4: The order of accuracy of the cuboid model evaluated with results from the transient laminar channel flow. The theoretical solutions are used as the benchmark. Results are calculated at $t\nu/H^2 = 1$. The streamwise velocity v is examined.

Resolutions	$v\,(L1)$	order	$v\,(L2)$	order
$10 \times 2 \times 2$	1.658E-2	(−)	1.521E-2	(−)
$20 \times 4 \times 4$	4.577E-3	1.857	4.183E-3	1.862
$40 \times 8 \times 8$	1.354E-3	1.757	1.236E-3	1.759
$80 \times 16 \times 16$	4.426E-4	1.613	4.040E-4	1.613
Averaged		1.742		1.745

Table 5: The order of accuracy of the cuboid model evaluated with the 3D decaying Taylor-Green vortex flow. Results of the cuboid model with a resolution of $512 \times 640 \times 640$ are used as the benchmark to compute the error norms of the cuboid model at lower grid resolutions. Results are calculated at $2\pi U_0 t/L = 3$.

Resolutions	$u/v/w\,(L1)$	order $u/v/w$	$u/v/w\,(L2)$	order $u/v/w$
$32 \times 40 \times 40$	2.805E-2/2.263E-2/4.009E-2	(−)	3.439E-2/2.458E-2/4.336E-2	(−)
$64 \times 80 \times 80$	6.162E-3/4.309E-3/8.224E-3	2.187/2.393/2.285	7.242E-3/4.881E-3/9.262E-3	2.248/2.332/2.227
$128 \times 160 \times 160$	1.172E-3/8.336E-4/1.583E-3	2.394/2.370/2.377	1.356E-3/1.010E-3/1.904E-3	2.417/2.273/2.282
$256 \times 320 \times 320$	2.352E-4/2.101E-4/3.224E-4	2.317/1.988/2.287	2.541E-4/2.341E-4/3.930E-4	2.416/2.109/2.276
Averaged		2.299/2.250/2.316		2.360/2.238/2.262

lower resolutions. Using the results of the cuboid grid at the highest-resolution as a benchmark has another benefit, namely, the initial flow conditions are identical at the mesoscopic level due to the same initialization method used.

In order to measure the order of accuracy, the $L1$ and $L2$ errors are calculated as

$$\epsilon_{L1}(t) = \frac{\sum_{x,y,z} |q_n(x,y,z,t) - q_b(x,y,z,t)|}{\sum_{x,y,z} |q_b(x,y,z,t)|}, \tag{36a}$$

$$\epsilon_{L2}(t) = \frac{\sqrt{\sum_{x,y,z} |q_n(x,y,z,t) - q_b(x,y,z,t)|^2}}{\sqrt{\sum_{x,y,z} |q_b(x,y,z,t)|^2}}. \tag{36b}$$

where $q_n(x,y,z,t)$ and $q_b(x,y,z,t)$ represent the numerical value and corresponding benchmark value of a quantity at location (x,y,z) and time t. For each quantity, the $L1$ and $L2$ error norms for velocity at different grid resolutions are calculated according to Eq. (36). The order of accuracy could be estimated based on either $L1$ or $L2$ error norms. Assume the error norm calculated from one given resolution is $\epsilon_0(t)$, as we increase the resolution by a factor of m in each direction, the new error norm should be smaller and is denoted by $\epsilon_m(t)$. Then the order of accuracy n is estimated as

$$n(t) = log_m\left(\frac{\epsilon_0(t)}{\epsilon_m(t)}\right). \tag{37}$$

The order of accuracy is first checked by laminar flow at $t\nu/H^2 = 1$. Only the streamwise velocity v are examined because the other two velocity components are always zero in the laminar channel flow. The results are compiled in Table 4, showing that the order of accuracy is between 1.6 to 1.8. That is because the laminar channel flow can be easily well resolved. Thus, increasing the grid resolution has a less significant effect on the error norm especially when the resolution is already high enough.

For the case of the 3D decaying Taylor-Green vortex flow, the results of error norms computed from each velocity component are compiled in Table 5 and Table 6, for two different times, $2\pi U_0 t/L = 3$ and 5, respectively. The results clearly demonstrated that the order of accuracy is around 2.

In addition, the $L1$ and $L2$ error norms with different aspect ratios are also compared to study if the error norms are dependent on the aspect ratio. Four laminar flow cases listed in Table 1 are used at the same resolution of $40 \times 2 \times 2$.

Table 6: The order of accuracy of the cuboid model evaluated with the 3D decaying Taylor-Green vortex flow. Results of the cuboid model with a resolution of $512 \times 640 \times 640$ are used as the benchmark to compute the error norms of the cuboid model at lower grid resolutions. Results are calculated at $2\pi U_0 t/L = 5$.

Resolutions	$u/v/w\,(L1)$	order $u/v/w$	$u/v/w\,(L2)$	order $u/v/w$
$32 \times 40 \times 40$	1.001E-1/1.043E-1/1.128E-1	(–)	1.261E-1/1.239E-1/1.210E-1	(–)
$64 \times 80 \times 80$	2.104E-2/2.005E-2/2.485E-2	2.250/2.379/2.182	2.969E-2/2.876E-2/3.465E-2	2.087/2.107/1.804
$128 \times 160 \times 160$	4.143E-3/3.279E-3/4.641E-3	2.344/2.612/2.421	6.044E-3/5.222E-3/6.706E-3	2.296/2.461/2.369
$256 \times 320 \times 320$	6.619E-4/5.503E-4/8.162E-4	2.646/2.575/2.507	1.049E-3/8.904E-4/1.237E-3	2.526/2.552/2.439
Averaged		2.413/2.522/2.370		2.303/2.373/2.204

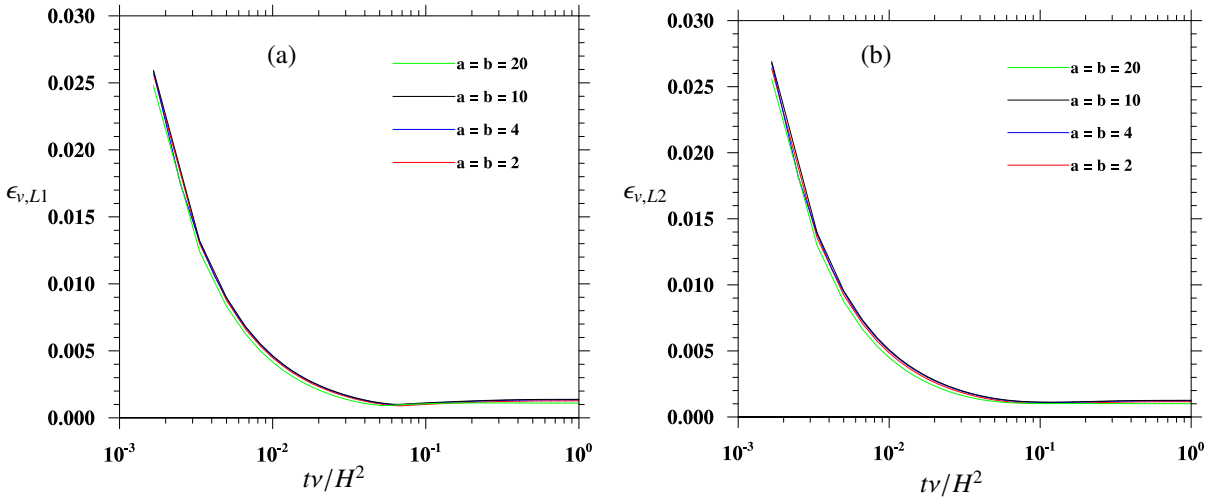

Figure 8: (a) The $L1$ error norm and (b) the $L2$ error norm of the streamwise velocity v in the laminar channel flow simulations. Results from four different aspect ratios are compared.

The $L1$ and $L2$ error norms of streamwise velocity v are compared in Fig. 8. We can conclude that when aspect ratios a and b are both larger than one, the error norms are independent of the aspect ratio since the smallest lattice spacing is $\delta_x = 1$. However, as stated in Sec. 3.1, the numerical error in laminar channel flow depends on the aspect ratio if the smallest lattice spacing is smaller than one, namely, when a or $b < 1$.

3.4. Turbulent channel flow

The final test case is the turbulent channel flow, which is a canonical wall-bounded turbulent flow [29, 30, 31]. This is a time-dependent and three-dimensional flow. The flow is also highly inhomogeneous and anisotropic, especially in the near-wall region. Like the laminar channel flow, the turbulent channel flow is also bounded by two parallel flat walls. Again, x, y, and z represent the transverse, streamwise, and spanwise direction, respectively. At a sufficiently high flow Reynolds number, the flow may transit from a laminar flow to a turbulent flow. In this paper, we only focus on the fully developed stage of turbulent channel flow which have been documented extensively, both in terms of direct numerical simulations and experimental measurements [33, 34, 31].

In this first simulation of a turbulent channel flow using the cuboid model, the domain size is set to $2H \times 4H \times 2H$, where H here is the channel *half* width. Although this domain is not very wide in the streamwise and spanwise directions, reasonable flow statistics can still be obtained as shown in our previous studies of particle-laden turbulent channel flows [37]. The periodic boundary condition is applied to both the streamwise (y) direction and the spanwise (z) direction. In the transverse (x) direction, again the mid-link bounce back (as described in Sec. 3.1) is applied to satisfy the no-slip boundary condition. In this simulation, 2D domain decomposition [32] is used to parallelize the code, and an efficient one-step two-array approach is used to integrate the collision and streaming sub-steps.

The simulation of turbulent channel flow could be divided into three stages:

Table 7: Parameter settings of the turbulent channel flow.

Aspect ratio	Re_τ	H	Domain size	$N_x \times N_y \times N_z$	ν	ν^V	u_τ	c_s	γ
$a = 1.25, b = 1$	180	100	$2H \times 4H \times 2H$	199×320×200	0.0036	0.1	0.00648	0.6325	-0.8

1. The initial excitation of turbulent fluctuations. Starting from an initial flow field, a non-uniform time-dependent perturbation force field is applied to the flow, in addition to the physical constant body force, to promote and accelerate velocity fluctuations in the flow.

2. Rapid transition to turbulent flow. Once velocity fluctuations in all the three directions have reached a certain level, the perturbation force field is then switched off. The constant body force can now sustain the turbulent fluctuations and the flow gradually evolves to a fully developed turbulent channel flow.

3. The fully developed turbulent channel flow. At this stage, the flow is statistically stationary, although the local flow structures continue to evolve in time. A simulation over a sufficiently long period of time can then be used to obtain average flow statistics such as the mean and turbulent r.m.s. velocity profiles.

In this simulation, the perturbation force is applied for 3 eddy turnover times. The eddy turnover time is defined as H/u_τ, where the friction velocity is $u_\tau = \sqrt{\tau_w/\rho_0}$, and τ_w is the average wall shear stress. The friction Reynolds number $Re_\tau = u_\tau H/\nu$ is set to 180, where ν is the kinematic shear viscosity. The wall length unit is defined as $\delta_\tau = \nu/u_\tau$. All quantities with superscript + are normalized by u_τ and δ_τ. The values of key parameters used for the turbulent channel flow are listed in Table 7. The two aspect ratios are set to $a = \delta_y/\delta_x = 1.25$ and $b = \delta_z/\delta_x = 1$, and $\delta_x = 1$ in lattice units. The half channel width H is set to $100\delta_x$. The domain size is $2H \times 4H \times 2H$, Since $\delta_y/\delta_x = 1.25$, thus for the same physical domain size the number of lattice nodes in the streamwise direction is 80% of the number used in the standard LBM model using the cubic lattice. Namely, the grid resolution for the cuboid lattice is $199 \times 320 \times 200$, compared to $199 \times 400 \times 200$ in the cubic lattice model [37].

The kinematic shear viscosity ν was set to 0.0036. The bulk viscosity ν^V is set to 0.1 to help maintain the numerical stability. This leads to a frictional velocity $u_\tau = 0.00648$. All relaxation parameters in Eq. (5) are set to 1.2. When simulating the turbulent channel flow with the cuboid model, we found that the numerical instability could occur for larger lattice aspect ratio. The reason for the numerical instability and methods to enhance numerical stability of the cuboid model should be studied in the future.

In Fig. (9a), the streamwise velocity v averaged over the whole domain is shown as a function of time. The result from the standard LBM model with the cubic lattice (taken from Wang *et al,* [37]), using the same physical parameters, initial flow field, and perturbation forcing is shown for comparison. The time evolutions of the averaged streamwise velocity based on the two models are identical for about 1.5 eddy turnover times. Then they become different at a given time due to inherent nonlinearity. Nevertheless, the evolutions remain similar qualitatively. Both reach the stationary stage after about 40 to 60 eddy turnover times. Thus, the statistic from 63 to 117.7 eddy turnover times are used to calculate the mean profiles at the stationary stage. The mean velocity averaged over $63 < tu_\tau/H < 117.7$ is 15.57 based on the cuboid model, compared to 15.67 from the cubic model. Both are within 0.5% of the value of 15.63 based on the spectral method [33]. All averaged profiles to be shown below are obtained time-averaging over the time interval of $63 < tu_\tau/H < 117.7$.

The mean streamwise-velocity profiles are compared in Fig. 9(b), where x^+ is the distance from the channel wall in wall units. At a given x, the streamwise velocity is averaged over the $y - z$ plane. Only the profiles over half of the channel are shown since they are symmetric. The linear viscous sublayer and the logarithmic region can be clearly identified. The result from the cuboid model is in excellent agreement with that from the cubic model, and they both agree with the spectral benchmark data taken from the literature [33, 34, 35, 36].

The corresponding profiles for the averaged Reynolds stress $-\langle u'v'\rangle/u_\tau^2$ are shown in Fig. 10(a), and these of root-mean-square (r.m.s.) fluctuation velocities are presented in Fig. 10(b). The results of the cuboid model are compared with the results from the standard cubic-lattice model and spectral benchmark data. Clearly, the cuboid model reproduces the same statistics and profiles of the cubic model. They both are in reasonable agreement with

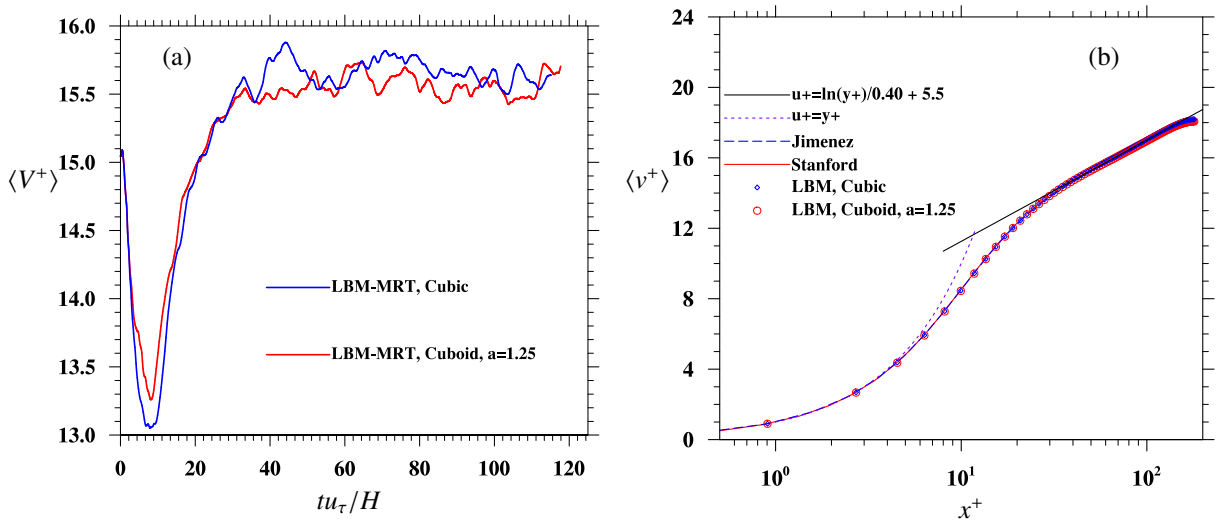

Figure 9: (a) The streamwise velocity averaged over the whole domain when the flow reaches the stationary stage. (b) Profiles of mean streamwise velocity as a function of x^+ when the flow reaches the stationary stage. All quantities are normalized as indicated.

the spectral benchmark data. There are also some differences in the streamwise and spanwise r.m.s. velocity profiles, which is related to the use of different domain size as discussed in Wang *et al.* [37, 38].

In summary, the cuboid lattice model is used, for the first time, to simulate the fully developed turbulent channel flow. The statistics of the fully developed flow are compared with the results from the cubic-lattice model in [37, 38] and previous spectral simulation data. All results are in good agreement. For the same physical domain size, the cuboid-lattice model with $\delta_y = 1.25\delta_x$ uses 20% less grid points in the streamwise direction when compared to the cubic-lattice model. With proper optimization of model parameters, we believe that larger aspect ratios could be used to further reduce the computational cost.

4. Summary and Conclusions

In this paper, a D3Q19 multiple-relaxation time lattice Boltzmann model on a cuboid lattice grid is developed through an inverse design analysis based on the Chapman-Enskog expansion. In this cuboid model, the lattice grid-lengths in the three spatial directions could be set to different values, namely, the aspect ratios a and b, defined as $a = \delta_y/\delta_x$, $b = \delta_z/\delta_x$, are input parameters of the cuboid model, where δ_x, δ_y and δ_z are the grid sizes in the three directions, respectively. In the model, the equilibrium moments are extended to include additional higher-order terms in order to address the anisotropy problem of viscosity coefficients due to the use of the cuboid lattice. This extension allows the proposed cuboid model to adopt the same transform matrix of the standard cubic model. A mesoscopic forcing term is also added to the lattice Boltzmann equation to realize the effect of macroscopic forcing.

In general, there are three important aspects to such non-standard LBM models: (a) full consistency with the Navier-Stokes equations, (b) numerical accuracy (whether the second-order accuracy is maintained), and (c) numerical stability and its dependence on the grid aspect ratio. To our knowledge, the new model represents one of the only three correct 3D models on a cuboid lattice, namely, the other two being the models of Hegele et al. (2013) and Jiang and Zhang (2014). We note that Hegele et al. (2013) used more lattice velocities (D3Q23) and they did not provide any meaningful numerical validation of 3D flow (the only validation in their paper was the propagation of cylindrical pressure wave). Jiang and Zhang (2014) did not demonstrate the second-order accuracy of their model and their numerical validations were limited to 3D laminar flows. The smallest aspect ratio used in their work was 0.82. In this paper, we developed a new model, provided a series of numerical validations (channel flow, 3D Taylor-Green, and turbulent channel flow). We also shown that the model has a second-order accuracy similar to standard LBM models.

To recover the correct hydrodynamic equations, the Chapman-Enskog expansion has been used to develop all

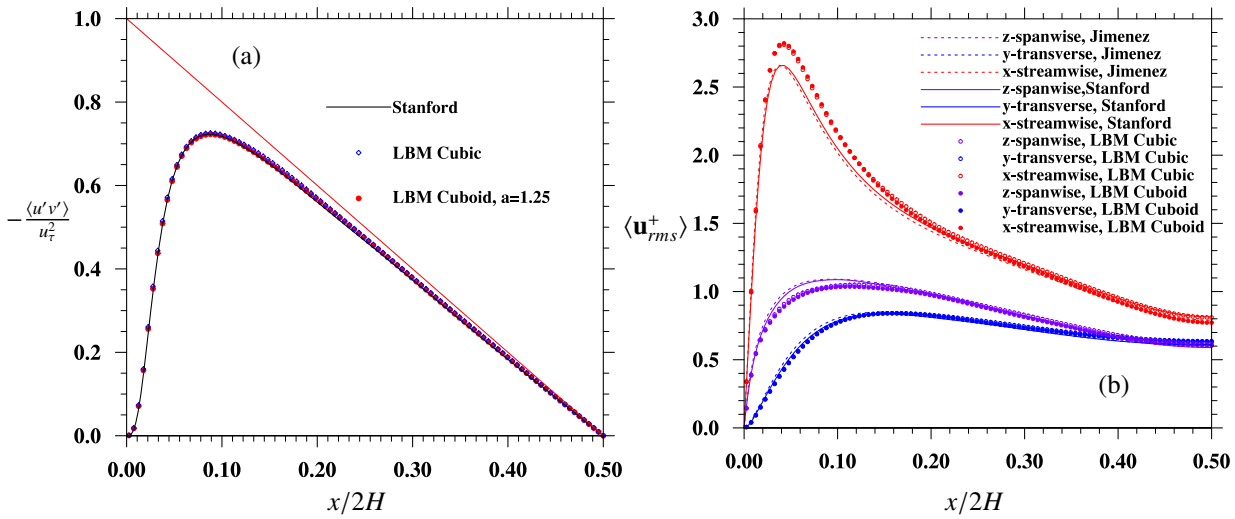

Figure 10: (a) The Reynolds stress $-\langle u'v'\rangle/u_\tau^2$ profiles and (b) the r.m.s. velocity profiles. All quantities are normalized as indicated.

constraints for the cuboid model. These constraints are then applied to design the zeroth to third-order equilibrium moments, and mesoscopic forcing terms. This inverse design process ensures a consistent and general cuboid model.

Based on the inverse design analysis shown in Sec. 2, 16 of the 19 zeroth-order equilibrium moments, 6 of the 19 first-order equilibrium moments, and 10 of the 19 mesoscopic forcing terms can be determined directly from the constraints resulting from the hydrodynamic equations. Clearly, further studies are needed to optimize those *free* terms that are not constrained by the hydrodynamic equations, in order to achieve a better numerical stability. It is also found that the first-order equilibrium moments offer two functions: (i) to resolve the anisotropy of viscosity coefficients associated with the use of the anisotropic lattice structure, and (ii) to adjust both shear and bulk viscosities independent of the relaxation parameters.

The cuboid model is then validated by three different benchmark cases, namely, the transient laminar channel flow, the 3D energy-cascading Taylor-Green vortex flow, and the fully developed turbulent channel flow. In all cases, results of the cuboid-lattice model are compared with the analytical solutions or results of other numerical methods. Good agreements are shown among these results, regardless of the aspect ratios used in the cuboid model.

With the proposed cuboid-lattice model, a smaller number of lattice points can be used to achieve the same result for an anisotropic flow such as the turbulent channel flow. This is because, compared to the standard cubic lattice, a relatively coarser lattice grid can be used in the direction where the flow variables vary more gradually (*i.e.*, , the streamwise direction of a channel or pipe). Thus, the overall computational efficiency can be improved.

Finally, we wish to comment on the range of grid aspect ratios that can be used in each non-standard model. In the 2D models of this kind, the minimum aspect ratio used in the previous studies is 0.45 in Bouzidi *et al.* [9], 0.5 in Zhou [11, 12], 2/3 in Hegele *et al.* [14]. Using the $\theta-$model [10], an aspect ratio of 0.3 could be used to simulate a 2D laminar lid-driven cavity flow and 2D Taylor-Green vortex flow. In a 2D model [16] using an extended equilibrium and MRT collision model, which is very similar to the current paper, an aspect ratio of 0.25 was used to simulate both 2D laminar lid-driven cavity flow and 2D Taylor-Green vortex flow. Another model [20] using an extended equilibrium and BGK collision model, an aspect ratio of 1/3 could be used to simulate 2D laminar flows. The above discussions indicate two aspects. First, for each non-standard model, there appears to be a limiting aspect ratio for numerical stability. Second, the study of Peng *et al.* [16] implies that aspect ratio below 0.8 could be used in our current cuboid model, as demonstrated in the case of laminar channel flow. The results of the current paper further demonstrates that, for the case of a turbulent flow, there seems to be a more strict requirement on the permissible range of aspect ratios for numerical stability.

For the 3D Taylor-Green vortex flow, we have attempted to use aspect ratios smaller than 0.80 for $Re_0 = 300$. In each case, the code became unstable eventually. We found that the instability first appears as noises in both the normal and shear stress modes as well as in the pressure mode. The noises grow in time, which leads to unphysical

velocity gradients and eventually excessive values of the extended components of the equilibrium moments. When Re_0 is reduced to 30, the cuboid model is stable for $a = b = 0.5$. At this moment, we have not fully understood the origin of numerical instability when simulating the 3D Taylor-Green vortex flow and the turbulent channel flow at relatively high flow Reynolds numbers. Namely, we have not found a method to optimize model parameters in order to ensure numerical stability at high flow Reynolds numbers. The logical approach would be to perform a systematic linear stability analysis of our cuboid model, as done for the standard LBM models [24, 39, 40, 41]. This is beyond the scope of the current paper and should be a topic for future research.

5. Acknowledgements

This work has been supported by the U.S. National Science Foundation (NSF) under grants CNS1513031, CBET-1235974, and AGS-1139743 and by Air Force Office of Scientific Research under grant FA9550-13-1-0213. LPW also acknowledges support from the Ministry of Education of P.R. China and Huazhong University of Science and Technology through Chang Jiang Scholar Visiting Professorship. The authors (LPW, HM, CP) would like to acknowledge the travel support from U.S. National Science Foundation (NSF) to attend ICMMES-2015, held in CSRC (www.csrc.ac.cn), Beijing, July 20 – 24, 2015, under the Grant CBET-1549614. Computing resources are provided by National Center for Atmospheric Research through CISL-P35751014, and CISL-UDEL0001 and by University of Delaware through NSF CRI 0958512.

6. Appendix

As mentioned in Sec. 2, the added part of equilibrium moments, $m_i^{(eq,1)}$, is composed of a set of 9 coefficients h_{ij}, λ, and the strain-rate tensor $(\partial_\beta u_\alpha + \partial_\alpha u_\beta)/2$. Therefore, we need to update the strain-rate components at each time step and apply them in the collision term. By design, all the strain-rate components can be calculated based on the non-equilibrium moments. The derivation is a bit tedious, we only present the final results here.

First, from Eq. (23) we observe that $\mathbf{m}^{(1)}$ is related to equilibrium moments and forcing. To separate the two, we define an array G_i as the part of $\mathbf{m}^{(1)}$ without any forcing involved. According to our derivation, we shall have $G_i = \mathbf{M}_{ij} f_j - m_i^{(eq,0)} + \delta_t \Psi_i / (2 - s_i)$, where $\mathbf{M}, m_i^{(eq,0)}, \Psi_i$ and s_i are defined in Sec. 2. Then, the strain-rate components can be calculated according to

$$\begin{cases} \partial_x u = (C_1 B_4 - C_2 B_2) / (B_1 B_4 - B_2 B_3), \\ \partial_y v = (C_2 B_1 - C_1 B_3) / (B_1 B_4 - B_2 B_3), \\ \partial_z w = \left[G_2 / \left(\rho_0 \delta_t c^2 \right) - r_{11} \partial_x u - r_{12} \partial_y v \right] / r_{13}, \\ \partial_y u + \partial_x v = G_{14} / c_1, \\ \partial_z v + \partial_y w = G_{15} / c_2, \\ \partial_z u + \partial_x w = G_{16} / c_3, \end{cases} \quad \begin{cases} B_1 = r_{11} r_{23} - r_{13} r_{21}, \\ B_2 = r_{12} r_{23} - r_{13} r_{22}, \\ B_3 = r_{23} r_{31} - r_{21} r_{33}, \\ B_4 = r_{23} r_{32} - r_{22} r_{33}, \\ C_1 = (r_{23} G_2 - r_{13} G_{10}) / \left(\rho_0 \delta_t c^2 \right), \\ C_2 = (r_{23} G_{12} - r_{33} G_{10}) / \left(\rho_0 \delta_t c^2 \right), \end{cases} \tag{38}$$

where $c_1 = \rho_0 \delta_t c^2 \lambda / a - a \rho_0 \delta_t c^2 \kappa_3 / (10 s_c)$, $c_2 = \rho_0 \delta_t c^2 \left[0.1 s_c^* \kappa_3 \left(a^2 b^2 - a^2 \right) + \lambda \right] / (ab) - ab \rho_0 \delta_t c^2 \kappa_3 / (10 s_c)$, $c_3 = \rho_0 \delta_t c^2 \left[0.1 s_c^* \kappa_3 \left(b^2 - a^2 \right) + \lambda \right] / b - b \rho_0 \delta_t c^2 \kappa_3 / (10 s_c)$, $s_c^* = (2 - s_c) / (2 s_c)$, and $\kappa_3 = \gamma + 4$. Other parameters have been defined in Sec. 2. The coefficients r_{ij} are given as

$$r_{ij} = h_{ij} + \begin{bmatrix} \left(19 \kappa_1 \frac{c_s^2}{c^2} - 30 - \frac{21 + 19\gamma}{5} \right) / s_e & \left(19 \kappa_1 \frac{c_s^2}{c^2} - 30 - \frac{21 + 19 a \gamma_a}{5} \right) / s_e & \left(19 \kappa_1 \frac{c_s^2}{c^2} - 30 - \frac{21 + 19 b \gamma_b}{5} \right) / s_e \\ \left[(3 - \kappa_1) \frac{c_s^2}{c^2} - \frac{6 - \gamma}{5} \right] / s_n & \left[(3 - \kappa_1) \frac{c_s^2}{c^2} + \frac{6 - a\gamma_a}{5} \right] / s_n & \left[(3 - \kappa_1) \frac{c_s^2}{c^2} + \frac{6 - b\gamma_b}{5} \right] / s_n \\ \kappa_2 \frac{c_s^2}{c^2} / s_n & \left(\kappa_2 \frac{c_s^2}{c^2} - \frac{6 - a\gamma_a}{10} \right) / s_n & \left(\kappa_2 \frac{c_s^2}{c^2} + \frac{6 - b\gamma_b}{10} \right) / s_n \end{bmatrix} \tag{39}$$

where $\kappa_1 = 1/a^2 + 1/b^2 + 1$, $\kappa_2 = 1/a^2 - 1/b^2$, $\gamma_a = a(\gamma + 4) - 4/a$, $\gamma_b = b(\gamma + 4) - 4/b$ and h_{ij} are defined in Eq. (27).

References

[1] S. Chen, G. D. Doolen, Lattice Boltzmann method for fluid flows, Annual Review of Fluid Mechanics 30 (1) (1998) 329-364.
[2] S. Succi, The Lattice-Boltzmann Equation, Oxford University Press, Oxford, 2001.
[3] Z. Guo, C. Shu, Lattice Boltzmann method and its applications in engineering (advances in computational fluid dynamics),World Scientific Publishing Company, 2013.
[4] He X., Luo L.-S., Dembo M., Some progress in lattice Boltzmann method. Part I. Nonuniform mesh grids, J. Comp. Phys., 129 (1996) 357–363.
[5] Niu X.D., Chew Y.T., Shu C., Simulation of flows around an impulsively started circular cylinder by Taylor series expansion and least squares-based lattice Boltzmann method, J. Comp. Phys., 188 (2003) 176–193.
[6] Filippova O., Hänel, Boundary-fitting and local grid refinement for lattice-BGK models, Int. J. Modern Phys. C, 9 (1998) 1271–1279.
[7] Cao N., Chen S., Jin S., et al, Physical symmetry and lattice symmetry in the lattice Boltzmann method, Phys. Rev. E, 55 (1997) R21-R24.
[8] Bardow A., Karlin I. V., Gusev A. A., General characteristic-based algorithm for off-lattice Boltzmann simulatiions, Europhys. Lett., 73 (2006) 434–440.
[9] Bouzidi M., dHumi'eres D., Lallemand P., et al, Lattice Boltzmann Equation on a two-dimensional rectangular grid, J. Comp. Phys. 172 (2001) 704–717.
[10] Zong Y., Peng C., Z. Guo, et al, Designing Correct Fluid Hydrodynamics on A Rectangular Grid using MRT Lattice Boltzmann Approach, Comp.& Math. Applications, (2015), DOI: 10.1016/j.camwa.2015.05.021.
[11] Zhou J., Rectangular lattice Boltzmann method, Phys. Rev. E, 81(2010) 026705.
[12] Zhou J., MRT rectangular lattice Boltzmann method, Inter. J. Modern Phys. C, 23 (2012) 1250040.
[13] Chikatamarla S., Karlin I., Comment on Rectangular lattice Boltzmann method, Phys. Rev. E., 83 (2011) 048701.
[14] Hegele L. Jr., Mattila K., Philippi P., Rectangular lattice Boltzmann schemes with BGK-collision operator, J Sci. Comput., 56 (2013) 230–242.
[15] Jiang B., Zhang X., An Orthorhombic Lattice Boltzmann Model for Pore-Scale Simulation of Fluid Flow in Porous Media, Transp. Porous Med. (2014) 104:145–159.
[16] Peng et al., 2016, A hydrodynamically-consistent MRT lattice Boltzmann model on a 2D rectangular grid, submitted to J. Comp. Phys.
[17] Inamuro T., A lattice kinetic scheme for incompressible viscous flows with heat transfer, Phil. Trans. R. Soc. Lond. A, 360 (2002) 477–484.
[18] Yoshino M., Hotta Y., Hirozane T.,*et al.* , A numerical method for incompressible non-Newtonian fluid flows based on the lattice Boltzmann method, J Non-Newton. Fluid Mech., 147 (2007) 69–78.
[19] Wang L., Mi J., Meng X., *et al.* , A localized mass-conserving lattice Boltzmann approach for non-Newtonian fluid flows, Commun. Comput. Phys., 17 (2015) 908–924.
[20] Peng et al., 2016, A lattice-BGK model for the Navier-Stokes equations based on a rectangular grid, submitted to Comp.& Math. Appl.
[21] He X., Zou Q., Luo L.-S., Dembo M., Analytic solutions of simple flows and analysis of nonslip boundary conditions for the lattice Boltzmann BGK model. Journal of Statistical Physics, Vol. 87, Nos. 1/2, 1997.
[22] Taylor, G.I. and Green, A.E., 1937, Mechanism of the production of small eddies from large ones. Proc. Royal Soc. London, A, 158: 499-521.
[23] D. d'Humieres, I. Ginzburg, M. Karfczyk, *et al.* , Multiple-relaxation-time lattice Boltzmann models in three dimensions, Phil. Trans. R. Soc. Lond. A (2002) 360, 437–451.
[24] Lallemand P., Luo L.S., Theory of the lattice Boltzmann method: Dispersion, dissipation, isotropy, Galilean invariance, and stability, Phys. Rev. E 61 (2000) 6546.
[25] X. He, L.-S. Luo, Theory of the lattice Boltzmann method: From the Boltzmann equation to the lattice Boltzmann equation, Phys. Rev. E 56 (1997) 6811.
[26] Inamuro T., A lattice kinetic scheme for incompressible viscous flows with heat transfer, Phil. Trans. R. Soc. Lond. A, 360 (2002) 477–484.
[27] Min et al., 2016, An inverse design analysis of mesoscopic implementation of non-uniform forcing in MRT lattice Boltzmann models, submitted to Comp.& Math. Appl.
[28] X. He, Q. Zou, and L.-S. Luo, Analytic solutions of simple flows and analysis of nonslip boundary conditions for the lattice Boltzmann BGK model, J. Stat. Phys. 87 (1997) 115.
[29] Amati G., Succi S., Piva R., Massively parallel lattice-Boltzmann simulation of turbulent channel flow, Int J Mod Phys C, 8 (1997): 869–878.
[30] Toschi F., Amati G., Succi S., Benzi R., Piva R., Intermittency and structure functions in channel flow turbulence, Phys Rev Lett, 82 (1999): 5044–7.
[31] P. Lammers, K.N. Beronov, R. Volkert, G. Brenner, F. Durst, Lattice BGK direct numerical simulation of fully developed turbulence in incompressible plane channel flow, Computers & Fluids, 35 (2006) 1137–1153.
[32] H. Gao, C. Q. Qiu, D. Fan, Y. Jin, L-P. Wang, 2010, Three-dimensional microscale flow simulation and colloid transport modeling in saturated soil porous media, Comp.& Math. Appl., 59 (2010): 2271–2289.
[33] Kim, J., Moin, P., and Moser, R., Turbulence Statistics in Fully-Developed Channel Flow at Low Reynolds-Number, J. FluidMech., 177 (1987) 133-166.
[34] Moser, R., Kim, J., and Mansour, N. N., Direct Numerical Simulation of Turbulent Channel Flow up to Re-Tau = 590, Phys. Fluids., 11 (1999) 943-945.
[35] S. Hoyas, J. Jimenez, Reynolds number effects on the Reynolds-stress budgets in turbulent channels, Phys. Fluids, 20 (2008) 101511.
[36] J. Jimenez, S. Hoyas, Turbulent fluctuations above the buffer layer of wall-bounded flows, J. Fluid Mech. 611 (2008) 215-236.
[37] Wang L-P, Peng C, Guo ZL, Yu ZS, Flow Modulation by Finite-Size Neutrally Buoyant Particles in a Turbulent Channel Flow, ASME J. of Fluids Engr., 138 (2016) 041103.
[38] Wang L-P, Peng C, Guo ZL, Yu ZS, Lattice Boltzmann Simulation of Particle-Laden Turbulent Channel Flow, Computers and Fluids, 124 (2016) 226-236.
[39] J. D. Sterling and S. Chen, 1996, Stability analysis of lattice Boltzmann methods, J. Comput. Phys. 123, 196–206 (1995).
[40] R.A. Worthing, J. Mozer, G. Seeley, Stability of lattice Boltzmann methods in hydrodynamic regimes, Phys. Rev. E 56 (1997) 2243–2253.

[41] X.D. Niu, C. Shu, Y.T. Chew, T.G. Wang, Investigation of stability and hydrodynamics of different lattice Boltzmann models, J. Stat. Phys. 117 (3–4) (2004) 665–680.